communications biology

ARTICLE

https://doi.org/10.1038/s42003-021-02583-3 OPEN

TC10 regulates breast cancer invasion and metastasis by controlling membrane type-1 matrix metalloproteinase at invadopodia

Maren Hülsemann[1,2], Colline Sanchez[1,2], Polina V. Verkhusha[1], Vera Des Marais[1,2,3], Serena P. H. Mao[1], Sara K. Donnelly[1], Jeffrey E. Segall[1,2] & Louis Hodgson[1,2]✉

During breast cancer metastasis, cancer cell invasion is driven by actin-rich protrusions called invadopodia, which mediate the extracellular matrix degradation required for the success of the invasive cascade. In this study, we demonstrate that TC10, a member of a Cdc42 subfamily of p21 small GTPases, regulates the membrane type 1 matrix metalloproteinase (MT1-MMP)-driven extracellular matrix degradation at invadopodia. We show that TC10 is required for the plasma membrane surface exposure of MT1-MMP at these structures. By utilizing our Förster resonance energy transfer (FRET) biosensor, we demonstrate the p190RhoGAP-dependent regulation of spatiotemporal TC10 activity at invadopodia. We identified a pathway that regulates invadopodia-associated TC10 activity and function through the activation of p190RhoGAP and the downstream interacting effector Exo70. Our findings reveal the role of a previously unknown regulator of vesicular fusion at invadopodia, TC10 GTPase, in breast cancer invasion and metastasis.

[1] Department of Anatomy and Structural Biology, Albert Einstein College of Medicine, Bronx, NY 10461, USA. [2] Gruss-Lipper Biophotonics Center, Albert Einstein College of Medicine, Bronx, NY 10461, USA. [3] Analytical Imaging Facility, Albert Einstein College of Medicine, Bronx, NY 10461, USA. ✉email: louis.hodgson@einsteinmed.org

Cancer metastasis represents a multistep process, during which cells escape from a primary tumor and disseminate throughout the body, establishing new tumors at distant sites. To achieve this dissemination, cancer cells form actin-rich protrusions called invadopodia. The invadopodia structures have been identified in patient-derived tumor cells[1], and several breast cancer animal models show the presence of protrusive structures positive for invadopodia markers during the invasion, in vivo[2–5]. Importantly, recent studies indicate that invadopodia are required for cancer metastasis at sites of tumor cell intravasation[6,7] and extravasation[8–10], in vivo, underpinning their importance during several key stages of cancer, including tumor invasion and dissemination[11].

Mature invadopodia degrade the extracellular matrix (ECM) by recruiting membrane type 1 matrix metalloproteinases (MT1-MMP), a transmembrane protease that has been associated with ECM degradation during mammary adenocarcinoma invasion[12]. Invadopodia structures are spatially and temporally regulated[13] and are necessary to breach the basement membrane[14] and degrade the ECM during the intra/extravasation process[15–20]. Although the therapeutic efficacy of proteinase inhibitors has not been successfully established in clinical applications[21,22], in vitro and in vivo studies have indicated that MT1-MMP-mediated functions play important roles during the breast tumor metastatic cascade. These issues highlight our lack of clear understanding regarding the mechanisms that underlie the tumor invasion and dissemination processes, preventing the delineation of the contributions made by proteinase-dependent[23–25] and -independent[26] processes during tumor invasion and metastasis.

TC10 is a p21 small GTPase that belongs to the Rho family and is closely related to Cdc42, a canonical small GTPase. The role played by Cdc42 in the regulation of invadopodia generation has previously been demonstrated[24,27]. A minor paralog of Cdc42, TC10, has not yet been established as a key player in tumor invasion and metastasis[28–31], although the involvement of TC10 has been recognized in other diseases, including diabetes[32]. In general, Rho-family GTPases serve as molecular switches that cycle between the GTP-bound on state and the GDP-bound off state. GTPases are regulated by guanine nucleotide exchange factors (GEFs), which exchange GDP for GTP, GTPase-activating proteins (GAPs), which catalyze GTP hydrolysis, and guanine nucleotide dissociation inhibitors (GDIs), which can prevent the GDP to GTP exchange. Unlike other canonical Rho GTPases, TC10 has a relatively low binding affinity for Mg^{2+}, suggesting that wild-type (WT) TC10 may act as a fast-cycling GTPase, remaining in an activated state unless acted upon by GTPase regulators, such as GAPs[33,34,98]. TC10 is highly active on exocytic vesicles and recycling endosomes, and the TC10-mediated hydrolysis of GTP is necessary to promote vesicular fusion at the plasma membrane[35]. TC10 interacts with Exo70 as part of a conserved, octameric exocyst complex that recruits TC10-loaded vesicles to the plasma membrane[36,37]. This function of TC10 is conserved in neurites[38], suggesting that TC10 activity is broadly important for exocytosis. The docking of the exocyst complex at invadopodia has been observed in breast cancer cells, where it appears to control the exocytic presentation of MT1-MMP[39]. These observations indicate the likely involvement of a yet unknown vesicular fusion regulator that may be necessary to complete the final step of MT1-MMP surface presentation at tumor invadopodia[40].

In this study, we showed that endogenous TC10 is localized at invadopodia and that TC10 depletion markedly reduced ECM degradation and the in vitro invasion of mammary adenocarcinoma cells. We identified an important control node for the TC10 GTPase function involving p190RhoGAP, which is necessary for the regulation of TC10 activity at invadopodia. We observed the activation dynamics of TC10 at invadopodia using our Förster resonance energy transfer (FRET)-based TC10 biosensor. Importantly, we demonstrated that the TC10-mediated hydrolysis of GTP catalyzed by p190RhoGAP, was required for matrix degradation and the surface exposure of MT1-MMP at invadopodia. Moreover, we showed that TC10 significantly impacts breast tumor metastasis to the lungs in an in vivo mouse orthotopic model of breast cancer metastasis. Taken together, our results indicated an important role for TC10 as a regulator of exocytic vesicular control at invadopodia, involved in matrix degradation, invasion, and metastasis of breast cancer.

Results

TC10 is localized at invadopodia and regulates ECM degradation function of invadopodia. TC10 is known to function in vesicular trafficking, especially during glucose receptor transport in diabetes[41]; however, its role in cancer has not yet been elucidated. We hypothesized that TC10 might impact cancer invasion and metastasis by regulating the functions of tumor invadopodia. We found that endogenous TC10 was localized at invadopodia in two different breast cancer cell lines: rat adenocarcinoma MTLn3 (Fig. 1a) and human triple-negative MDA-MB-231 (Supplementary Fig. 1). Endogenous TC10 at invadopodia displayed two distinct localization patterns, either laterally at the sides of invadopodia or within the core of invadopodia, overlapping with the cortactin/Tks5 core marker proteins (Fig. 1b, c; Supplementary Fig. 1). Under steady-state conditions in fixed cells, TC10 localized predominantly to the invadopodia core (Fig. 1c). To characterize TC10 localization during the early phases of invadopodia formation, we serum-starved MTLn3 cells and then stimulated them with epidermal growth factor (EGF) to induce the synchronous formation of invadopodium precursors, which are unable yet to degrade the ECM. We found that TC10 was initially partitioned equally between the core and the regions surrounding the core, whereas 5 min after EGF stimulation, TC10 was observed to accumulate at the core (Fig. 1d). This timing relative to EGF stimulation coincided with previous observations regarding β1 integrin activation dynamics during EGF-stimulated invadopodia precursor formation[42] and with the activation of various pathways associated with this important adhesion molecule[43]. These observations may indicate the possible involvement of a β1 integrin-adhesion-mediated pathway in the modulation of TC10 activity and functions at invadopodia.

We next visualized the dynamics of TC10 recruitment at invadopodia by live-cell total internal reflection fluorescence (TIRF) microscopy, set up to achieve a modest HiLo-illumination. We observed dynamic fluctuations in TC10 localization between the core and the region surrounding the core, and importantly what appeared to be local fusions of TC10 from vesicle-like structures enriched in TC10 merging at the sites of invadopodia (Fig. 1e; Supplementary Movie 1). The movements of structures enriched in TC10 showed dynamic motions reminiscent of vesicular trafficking, which also overlapped with MT1-MMP-mCherry[44] both during trafficking and at invadopodia (Fig. 1f, g; Supplementary Movies 2 and 3). The apparent vesicular localization of TC10 and colocalization with structures containing MT1-MMP, which are known to be trafficked via exocytic vesicles[45,46], prompted us to characterize the vesicular compartments of TC10 localization, similar to what had been done previously at the leading edge of a different cell line[35]. The colocalization analysis indicated that TC10 was most strongly overlapping with the exocytic vesicular compartment labeled by VSVg-EGFP but not with NPY, with additional overlaps with endosomes (Rab5A and Rab7A) and recycling compartments (Rab11A and Transferrin Receptor) (Supplementary Fig. 2).

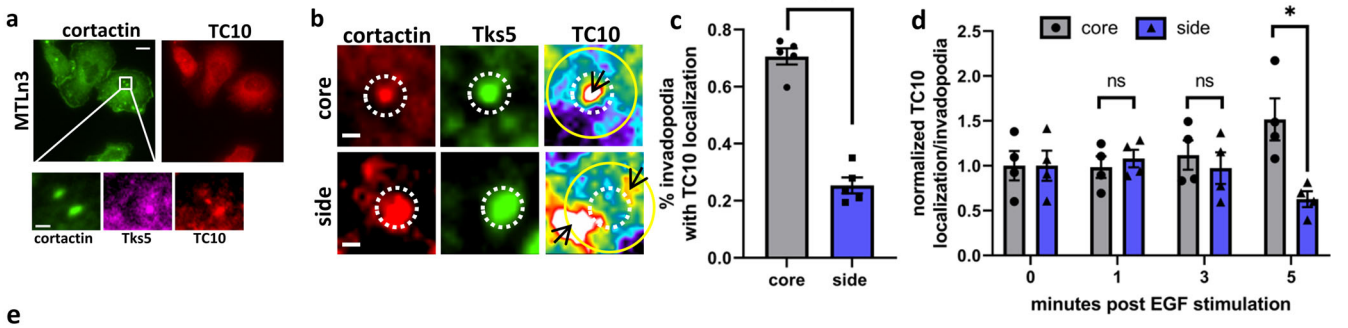
a
cortactin
TC10
MTLn3
cortactin
Tks5
TC10
b
cortactin
Tks5
TC10
core
side
c
**
% invadopodia with TC10 localization
0.8
0.6
0.4
0.2
0.0
core
side
d
core
side
*
ns
ns
normalized TC10 localization/invadopodia
2.5
2.0
1.5
1.0
0.5
0.0
0
1
3
5
minutes post EGF stimulation

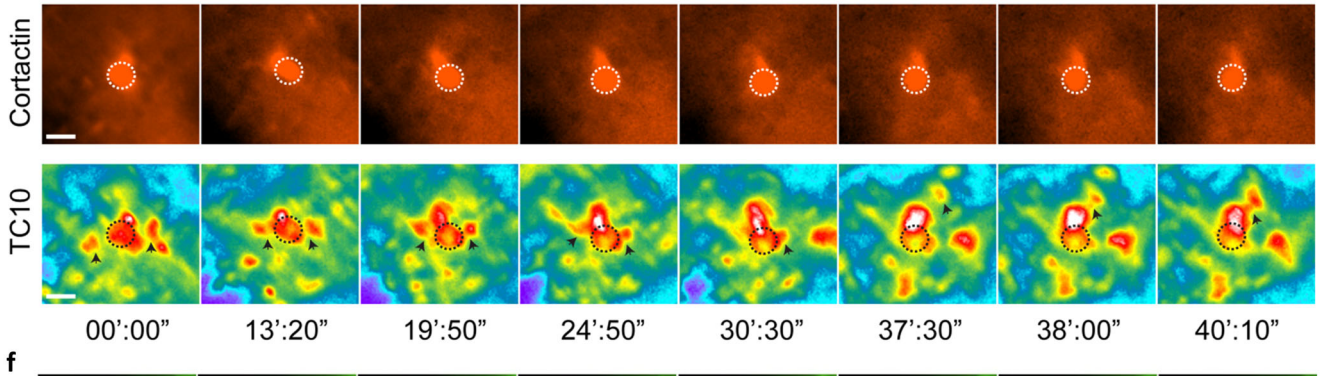
e
Cortactin
TC10
00':00"
13':20"
19':50"
24':50"
30':30"
37':30"
38':00"
40':10"

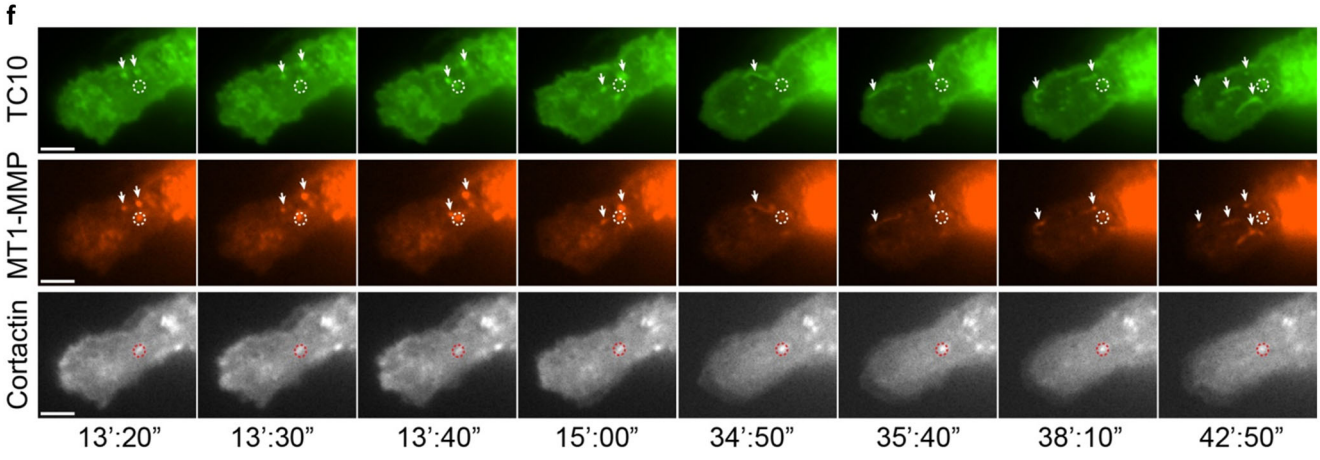
f
TC10
MT1-MMP
Cortactin
13':20"
13':30"
13':40"
15':00"
34':50"
35':40"
38':10"
42':50"

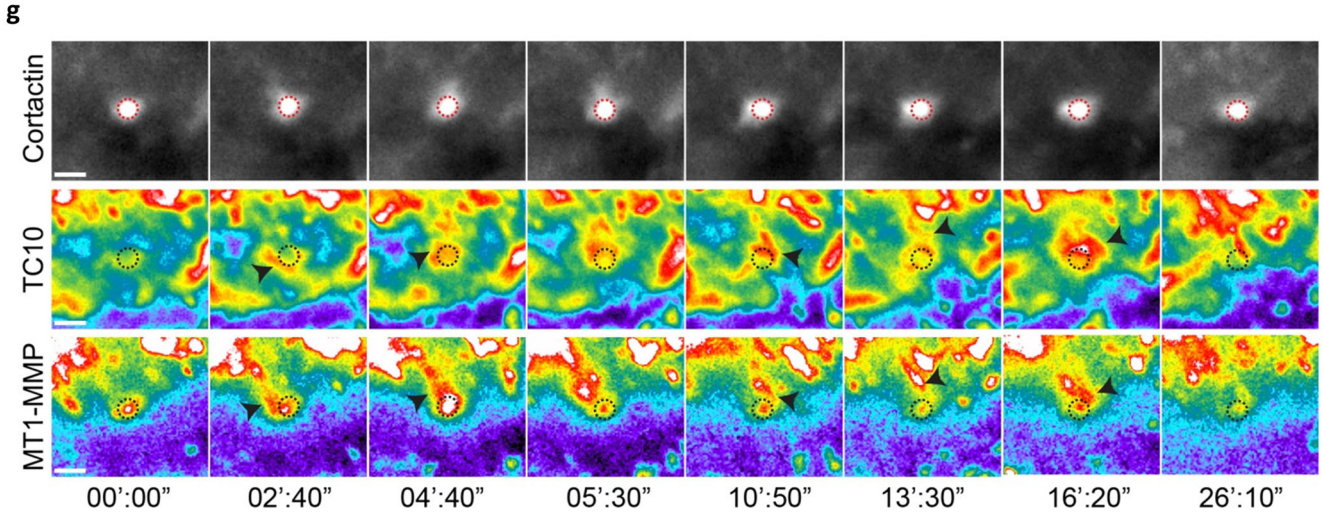
g
Cortactin
TC10
MT1-MMP
00':00"
02':40"
04':40"
05':30"
10':50"
13':30"
16':20"
26':10"

Fig. 1 TC10 is localized at invadopodia, vesicularly colocalized with MT1-MMP. a Representative localization of endogenous TC10 in rat mammary adenocarcinoma MTLn3 cells. Cortactin is shown to denote invadopodia structures. The white box area is enlarged to show colocalizations (bottom), showing cortactin, Tks5, and TC10 localizations. White bar = 10 μm (top); 2 μm (bottom). **b** Representative, enlarged view of the immunostaining of cortactin and Tks5 with TC10-WT-mCherry expression. White bar = 1 μm. The side localizations (yellow circle) were identified within a dilated circular region of approximately 30 pixels from the invadopodia core (dashed white circle). Black arrows point to TC10 localizations. **c** Quantification of mScarlet-TC10 WT localization at invadopodia structures. Student's *t*-test, two-tail analysis: $^{**}p = 0.001112$; $n = 5$ experiments; shown with SEM. **d** Quantification of TC10-WT-mCherry localization in MTLn3 cells stimulated with 5 nM EGF for the indicated times. Results were normalized to $t = 0$ min values for both side and core localized fractions. Student's *t*-test, two-tail analysis: ns $p = 0.5602$ for 1 min side versus core; $p = 0.5688$ for 3 min side versus core; $^{*}p = 0.01090$ for 5 min side vs. core; $n = 4$ experiments; shown with SEM. **e** Representative time-lapse panels of TC10 localizations at and near structures stained for cortactin to denote invadopodia in MTLn3 cells. The regions of interest showing apparent fusion-like events are marked with black arrowheads. Dotted circles show the position of the corresponding cortactin spot. White bar = 2 μm. Times are minutes':seconds". Also shown in Supplementary Movie 1. **f** Representative time-lapse panels of mNeonGreen-TC10 WT localizations together with MT1-MMP-mCh in cellular vesicular structures in MTLn3 cells. Colocalizations between TC10 and MT1-MMP are shown with white arrowheads. Dotted circles show the position of the corresponding cortactin spot. White bar = 5 μm. Times are minutes': seconds". Also shown in Supplementary Movie 2. **g** Representative time-lapse panels of mNeonGreen-TC10 WT and MT1-MMP-mCh at cortactin spots denoting invadopodia in MTLn3 cells. Points of interest and colocalizations around invadopodia are shown with black arrowheads. Dotted circles show the position of the corresponding cortactin spot. White bar = 2 μm. Times are minutes': seconds". Also shown in Supplementary Movie 3.

These results point to TC10 localization in trafficking vesicles, transient colocalizations with MT1-MMP at those structures, and dynamic coalescence of vesicles enriched in TC10 at invadopodia.

We next used small interfering RNA (siRNA) to deplete TC10 in MTLn3 cells, which resulted in reduced ECM degradation in these cells (Fig. 2a). The efficiency of TC10 genetic depletion with siRNA was approximately 50% in these cells (Supplementary Fig. 3); however, the observed impact on the phenotype was significant and could be rescued by the overexpression of a WT TC10 construct resistant to siRNA (Fig. 2b, c). A similar phenotype was observed in MDA-MB-231 cells even at a more modest efficiency of TC10 genetic depletion in those cells (Supplementary Figs. 4 and 5). The steady-state number of invadopodia was unaffected by TC10 depletion (Fig. 2d), suggesting roles of TC10 in regulating functions other than controlling the balance of formation or turnover rates of these structures. Corroborating this observation, the lifetimes (overall turnover rates) of invadopodia were not significantly impacted by TC10 depletion (Fig. 2e). Because TC10 has a documented role in vesicular fusion at the plasma membrane[35], and the invadopodium core protein cortactin plays important roles in vesicular regulation and secretion[47,48], we sought to determine if the invadopodia structures were impacted by depletion of TC10. Superresolution Stochastic Optical Reconstruction Microscopy (STORM) imaging of the cortactin core fluorescence indicated a significant reduction in the relative area ratios of the super-resolved cortactin core to the corresponding regions of interest at invadopodia measured in widefield epifluorescence (Fig. 2f, g). Interestingly, the cortactin epifluorescence images of the invadopodium core showed no difference in relative sizes, indicating that TC10 depletion resulted in diffuse cortactin core structures within an invadopodium without changing the overall size of the visible structures (Fig. 2h).

To explore the functional role of TC10 on its effects on matrix degradation, we overexpressed a TC10-Q75L mutant[35], which lacks the catalytic ability to hydrolyze GTP. The overexpression of TC10-Q75L resulted in an ECM degradation defect similar to that observed under TC10 depletion conditions (Fig. 2i), and no effect on the total number of invadopodia was observed (Fig. 2j). Overexpression of the wild-type TC10 had no effect on ECM degradation or the total number of steady-state invadopodia compared to the control (Fig. 2k, l). Moreover, the fractions of mature and degrading versus the immature and non-degrading invadopodia were no different from the control when the wild-type TC10 was overexpressed (Fig. 2m). Together, these observations indicated that the ability of TC10 to hydrolyze GTP and its GTPase cycling activity is necessary to regulate the ECM degradation function of invadopodia.

TC10 regulates MT1-MMP exposure at the plasma membrane of invadopodia. Because TC10 plays a well-known role in vesicular trafficking[35], in addition to the impacts on ECM degradation at invadopodia observed in the previous experiment, we hypothesized that TC10 regulates the MT1-MMP surface presentation at invadopodia by controlling vesicular fusion at the plasma membrane during exocytosis. To test this hypothesis, we first examined the endogenous localization of MT1-MMP at invadopodia and found two distinct patterns of localization: within the invadopodia core and laterally flanking the invadopodia core (Fig. 3a, b), with the side localization being more predominant (Fig. 3c, d). We then overexpressed in MTLn3 cells, an MT1-MMP with an enhanced green fluorescent protein (EGFP) tag on the cytoplasmic C-terminus and stained the surface-exposed MT1-MMP via antibody without permeabilizing the plasma membrane. When TC10 was depleted in these cells, we observed a significant reduction in the proportion of the surface-exposed MT1-MMP staining relative to the total MT1-MMP level, as measured by tracking the EGFP fluorescence intensity (Fig. 3e, f). No difference in total MT1-MMP levels at invadopodia was observed between the control and TC10-depleted cells (Fig. 3e, f). While the results suggest that the trafficking of MT1-MMP-containing vesicles or the loading of MT1-MMP cargo onto vesicles are likely not impacted by TC10 depletion, we wished to determine the extent of the endocytic recycling of MT1-MMP from the plasma membrane in our measurements. Since the C-terminus of MT1-MMP is required for recycling of MT1-MMP by endocytosis[49], we turned to an MT1-MMP construct containing an intramolecular fluorescent protein instead of the C-terminal fusion[50]. We exchanged the original mCherry in this construct[50] with a pH-sensitive, ratiometric pHLuorin2[51] and observed the ratio of green fluorescence emission in response to 400 nm vs. 470 nm excitation. We observed that fluorescence emission ratios at invadopodia were significantly reduced in TC10-depleted MTLn3 cells compared to the control, pointing to a reduction in the surface-exposed MT1-MMP at invadopodia in TC10-depleted cells (Fig. 3g, h). Moreover, we stained for endogenous MT1-MMP in MTLn3 cells using two different antibodies against MT1-MMP, with and without cell membrane permeabilization, and showed a reduced fraction of colocalization of the two MT1-MMP signals at invadopodia when TC10 was depleted (Supplementary Fig. 6). Together, these observations indicate that TC10 plays an

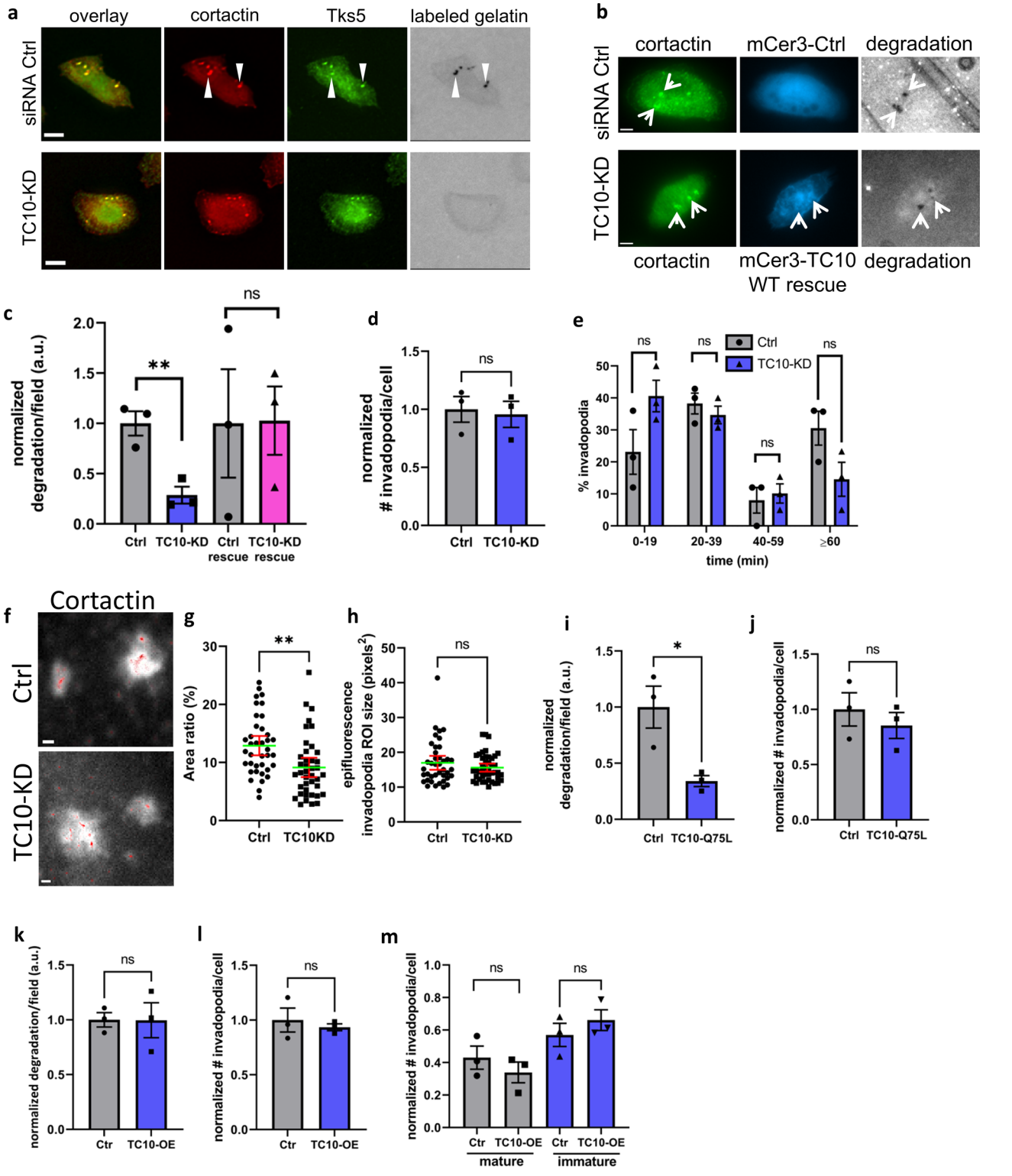

important role in the surface exposure of MT1-MMP at the plasma membrane, via the exocytic presentation of MT1-MMP at the plasma membrane. Moreover, the endocytic recycling likely influences the surface accumulation of MT1-MMP at invadopodia, as our staining assays indicated a small difference in the external to total staining ratio between the MT1-MMP-GFP construct versus the staining of the endogenous MT1-MMP.

Previously, the exocyst complex was observed to dock onto the lateral aspect of invadopodia, which was shown to be important for ECM degradation by invadopodia in breast cancer invasion[52]. Exo70 is a component of the octameric exocyst complex, which plays a critical role in vesicular docking at the cell membrane and is essential for the exocytic secretion of MMP at invadopodia[53]. Because TC10 has been shown to interact with Exo70[54], we examined the role played by the TC10–Exo70 interaction on MT1-MMP surface exposure and ECM degradation. We found that Exo70 localization strongly overlapped with TC10, both within the invadopodia core and at the lateral aspects of invadopodia (Fig. 3i, j). Unlike the MT1-MMP localization (Fig. 3c, d), Exo70 was predominantly localized with TC10 in the

Fig. 2 TC10 is required for matrix degradation at invadopodia. a Representative images from siRNA-mediated TC10 depletion in MTLn3 cells impacting gelatin matrix degradation, visualized using a 405 nm fluorescent gelatin matrix. Invadopodia are denoted by cortactin and Tks5 colocalization with spots of matrix degradation (arrows). White bar = 10 μm. **b** Representative images from siRNA-mediated TC10 depletion followed by rescue through overexpression of the wild-type mCerulean3-TC10 compared to its control (siRNA-Ctrl) expressing mCerulean3. White bar = 10 μm. Cortactin spots colocalizing with the fluorescent matrix degradation area are designated with arrowheads, indicating mature invadopodia. **c** Quantification of data shown in (**a**) and (**b**). Results are normalized against respective Ctrl. Student's *t*-test, one-tail analysis: $^{**}p = 0.004146$; two-tail analysis: ns $p = 0.9669$; $n = 3$ experiments; shown with SEM. **d** Total number of steady-state invadopodia/cell in TC10-depleted MTLn3 cells normalized to Ctrl MTLn3 cells. Student's *t*-test, two-tail analysis: $^{**}p = 0.7994$; $n = 3$ experiments; shown with SEM. **e** Invadopodia lifetimes in MTLn3 cells, shown as a histogram with bins corresponding to 20 min intervals. Student's *t*-test, two-tail analysis: ns, $p = 0.1106$ for 0–19 min; $p = 0.4472$ for 20–40 min; $p = 0.6922$ for 41–60 min; $p = 0.09957$ for >60 min; $n = 3$ experiments, shown with SEM. **f** Representative images of the superresolution projections of the cortactin localization within invadopodia in MTLn3 cells, with siRNA-control or siRNA-mediated TC10 depletion. White bar = 1 μm. Red spots are individual cortactin superresolution positions overlaid within the white areas which are the epifluorescence views of the cortactin core of invadopodia. **g** Quantification of (**f**), the relative area ratios of the superresolution projections to the corresponding regions of interest of the cortactin core fluorescence as determined in epifluorescence. $N = 3$ independent experiments, shown with mean +/− 95% confidence interval of the pooled data distribution, $^{**}p = 0.001890$, Student's *t*-test, two-tail analysis. **h** Quantification of the epifluorescence cortactin spot size (regions of interest) used to calculate the relative area ratios shown in (**g**). $N = 3$ independent experiments, shown with mean ± 95% confidence interval of the pooled data distribution, ns $p = 0.2285$, Student's *t*-test, two-tail analysis. **i** Overexpression of the GTP hydrolysis-deficient TC10 Q75L mutant in MTLn3 cells plated on a 405 nm fluorescent gelatin matrix, normalized to Ctrl overexpressing wild-type TC10. Student's *t*-test, paired one-tail analysis: $^{*}P = 0.01349$; $n = 3$ experiments; shown with SEM. **j** Total number of steady-state invadopodia in cells overexpressing wild-type TC10 or the Q75L mutant, normalized to the Ctrl overexpressing the wild-type TC10. Student's *t*-test, two-tail analysis: ns $P = 0.4824$; $n = 3$ experiments; shown with SEM. **k** Overexpression of WT TC10 has no effect on matrix degradation in MTLn3 cells. Student's *t*-test, paired two-tail analysis: ns $p = 0.9700$; $n = 3$ experiments; shown with SEM. **l** Overexpression of WT TC10 has no effect on the total number of steady-state invadopodia per cell in MTLn3 cells. Student's *t*-test, paired two-tail analysis: ns $p = 0.5835$; $n = 3$ experiments; shown with SEM. **m** Overexpression of WT TC10 has no effect on the relative numbers of the steady-state, mature versus immature invadopodia in MTLn3 cells. Student's *t*-test, paired two-tail analysis: ns $p = 0.5574$ for both comparisons; $n = 3$ experiments; shown with SEM. siRNA depletion characterizations are shown in Supplementary Figures 3 and 4.

invadopodia core. P29L/E31V/Y32H mutations in the switch I/II regions of Cdc42, which are important for effector interactions, have been shown previously to disrupt Cdc42–Exo70 co-immunoprecipitation[55,56]. When the corresponding, three-point mutations were introduced into TC10 (P43L/E45V/Y46H), we observed only a modest reduction in co-immunoprecipitation of Exo70 with TC10 (Lane 6: Fig. 3k). We then introduced two additional mutations, T49A and Y54C, to the triple mutant and called it 5×-mutation, or 5×mut. The T49A and Y54C mutations correspond to those in Cdc42 that affect activity status and effector interactions[57]. When the 5×mut-TC10 was co-expressed with Exo70, we saw an ablation of co-immunoprecipitation (Lane 7: Fig. 3k), indicating that these mutations further interfered with the complex formation. The GTP-hydrolysis-deficient (constitutively activated) mutant of TC10 (Q75L) modestly co-immunoprecipitated with Exo70, which was similar to the inactive dominant-negative T31N TC10 (Lanes 4 and 5: Fig. 3k). Interestingly, the F42L mutation corresponding to a mutation that renders other RhoGTPases GEF-independent and fast-cycling, resulted in the strongest co-immunoprecipitation of Exo70 (Lane 3: Fig. 3k). These results indicated that GTP hydrolysis and nucleotide cycling activity are important for an efficient TC10–Exo70 complex interaction and that mutating the residues P43L/E45V/Y46H/T49A/Y54C within the Switch I/II regions of TC10 destabilizes this complex interaction. We then used this 5×-mutated TC10, co-expressed with Exo70 in MTLn3 cells, and observed a significant impact on the ability of these cells to degrade the ECM (Fig. 3l), without affecting the total number of steady-state invadopodia (Fig. 3m). The expression of the 5×-mutated version of TC10 altered the relative localization patterns of Exo70 at invadopodia (Fig. 3n) but did not change the localization patterns of TC10 at invadopodia (Supplementary Fig. 7). We then wished to determine the extent of colocalization between TC10 and Exo70 at invadopodia. We used the Proximity Ligation Assay (PLA) and determined that the colocalization between TC10 and Exo70 was greater in the lateral/sides of invadopodia in WT TC10 compared to the 5× mutated TC10, as well as a significant increase in invadopodia that did not colocalize TC10 and Exo70 when 5×mutated TC10 was expressed (Fig. 3o, p). These observations indicated that the TC10-Exo70 complex is important for the appropriate targeting of Exo70 at invadopodia and that this interaction impacts ECM degradation. Furthermore, these results point to a potential mechanism through which MT1-MMP can be deposited into the plasma membrane as MT1-MMP-loaded vesicles containing TC10 approach the lateral/side aspect of invadopodia. GTP hydrolysis by vesicular-bound TC10 may begin to occur in this region, where TC10 first encounters a cognate GAP that resides within the invadopodium core, which facilitates GTP hydrolysis by TC10 to promote the plasma membrane fusion of the vesicles.

TC10 activity at invadopodia is spatially regulated. Because GTP hydrolysis is necessary for TC10-mediated vesicular fusion at the plasma membrane[35], we evaluated the activation dynamics of TC10 at and surrounding the invadopodia. For this purpose, we designed a FRET-based TC10 biosensor (Fig. 4a). The biosensor design is based on a monomeric, single-chain, and genetically encoded approach that is TC10-specific, similar to the design of our previous Rac and Cdc42 sensors[58,59]. The biosensor consists of a monomeric Cerulean 1 and monomeric circularly permuted (cp229) Venus fluorescent protein FRET pair with an optimized Rac/Cdc42-binder motif from our Rac/Cdc42 biosensors[58,60–62], and full-length TC10 attached at the C-terminus to maintain the GTPase-specific, native hypervariable region and the CAAX motif (Fig. 4a). As the size of the biosensor precluded in vitro purification, we tested and characterized the biosensor in HEK293 as previously described[63,64]. The spectrofluorometric characterization of the TC10 FRET biosensor in fixed and adhered HEK293T cells overexpressing the biosensor mutants revealed an approximately 80% difference in FRET/donor emission ratio between the constitutively activated (Q75L) and the off state (the dominant-negative T31N) of the TC10 biosensor (Fig. 4b). The WT version of the TC10 biosensor showed high FRET, similar to two different constitutively active TC10 biosensor mutants (G26V and Q75L, Fig. 4c), corroborating previous reports that WT TC10 represents an activated

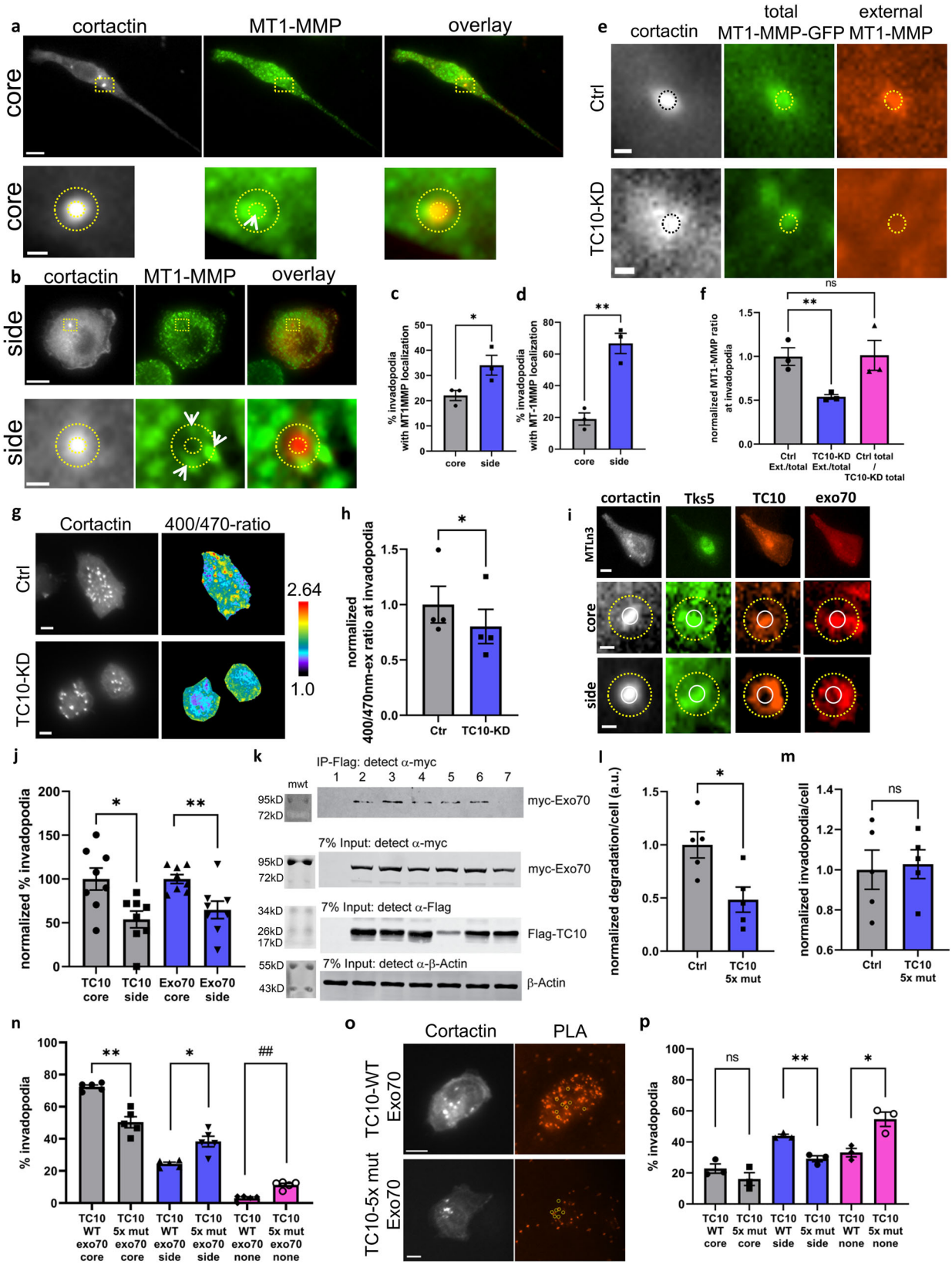

GTPase, due to a low Mg^{2+}-binding affinity[98]. We next asked if the cellular GEFs are required for the elevated activity of the WT TC10 biosensor when expressed. To probe the GEF-mediated activation of the WT TC10 biosensor, we first co-expressed the non-fluorescent dominant-negative T31N mutant of TC10 together with the WT TC10 biosensor to titrate away the cellular GEFs. The increasing titration of the dominant-negative TC10 expression reduced the biosensor activity to basal levels (Fig. 4d). This indicates that cellular GEFs are required for the activation of the TC10 biosensor; thus, the high activity of the WT TC10 biosensor is not only due to lower Mg^{2+} binding affinity that may bias toward a fast-cycling condition. Interestingly, the high

Fig. 3 TC10 regulates MT1-MMP exposure at the plasma membrane of invadopodia. a Representative images showing localization of endogenous MT1-MMP at invadopodia in MTLn3 cells, showing core-colocalized staining patterns of endogenous MT1-MMP and cortactin, shown with the zoomed views. **b** Representative images showing localization of endogenous MT1-MMP at invadopodia in MTLn3 cells, showing side-colocalized staining patterns of the endogenous MT1-MMP and the cortactin, shown with the zoomed views. In both (**a**) and (**b**), invadopodia are denoted by cortactin staining. The white bar in the whole-cell views = 10 μm; and zoomed views = 1 μm. Dotted concentric circles indicate the central core of invadopodium and the ring-like region defined by dilating the core region of interest by one diameter. **c** Quantification of endogenous MT1-MMP localization in MTLn3, either within the invadopodia core or on the lateral sides of the core. Student's *t*-test, one-tail analysis: $*p = 0.02632$; $n = 3$ experiments; shown with SEM. **d** MT1-MMP-GFP localization in MDA-MB-231, either within the invadopodia core or on the lateral sides of the core. Invadopodia cores are denoted by the colocalization of cortactin and Tks5 signals. Student's t-test, one-tail analysis: $**p = 0.001528$; $n = 3$ experiments; shown with SEM. **e** The extracellular surface presentation of MT1-MMP at invadopodia requires TC10 in MTLn3 cells. Representative images of the cortactin invadopodium core, colocalized with MT1-MMP-GFP signal and the extracellular labeling of MT1-MMP, in control versus TC10-KD. White bar = 1 μm. **f** Quantification of (**e**). The ratio between numbers of invadopodia with cytoplasmic (total) MT1-MMP and those featuring surface (ext.) MT1-MMP in cells treated with Ctrl (gray) or TC10 siRNA (blue). The ratio of total MT1-MMP-positive invadopodia counts in cells treated with Ctrl and TC10 siRNA (magenta), indicating that only the surface presentation of MT1-MMP is impacted by TC10 depletion. TC10-KD data are normalized to the Ctrl-ext. over total ratio. Student's *t*-test, one-tail analysis: $**p = 0.005750$; $n = 3$ experiments; shown with SEM. **g** Representative, ratiometric images of the MT1-MMP-pHLuorin2 in MTLn3 cells, with siRNA-mediated TC10 depletion. White bar = 5 μm. **h** Quantification of data shown in (**g**). Student's *t*-test, one-tail analysis: $*p = 0.01666$; $n = 3$ experiments; shown with SEM. **i** Representative, immunostaining of TC10 and Exo70 at the invadopodia site in MTLn3 cells, showing the side and the core localizations. The white bar in top = 10 μm; zoomed views = 1 μm. **j** The quantification of TC10 and exo70 localization at invadopodia in MTLn3 cells, as shown in (**i**), normalized to the core % for TC10 and Exo70, respectively. Student's *t*-test, two-tail analysis: $**p = 0.007508$; $*p = 0.01124$; $n = 8$ experiments; shown with SEM. **k** Immunoprecipitation of wild-type (WT) Exo70 and TC10 mutants, overexpressed in HEK293T cells. Lanes: 1, untransfected; 2, WT TC10; 3, F42L TC10; 4, Q75L TC10; 5, T31N TC10; 6, P43L/E45V/Y46H TC10; and 7, P43L/E45V/Y46H/T49A/Y54C (5× mut) TC10. Full-sized western blots are shown in Supplementary Figure 19. **l** Matrix degradation per cell comparing WT TC10 and 5× mut TC10 overexpression in MTLn3 cells, as plated on a 405 nm fluorescent gelatin matrix. Results are normalized to the Ctrl. Student's *t*-test, paired one-tail analysis: $**p = 0.005604$; $n = 5$ experiments; shown with SEM. **m** Total number of steady-state invadopodia, comparing WT TC10 and 5× mut TC10, overexpressed in MTLn3 cells. Results are normalized to the Ctrl. Student's *t*-test, paired two-tail analysis: ns $p = 0.7283$; $n = 5$ experiments; shown with SEM. **n** Localization of exo70 at invadopodia (core/side/no localization) in MTLn3 cells, comparing the overexpression of WT TC10 and 5× mut TC10. Student's *t*-test, paired two-tail analysis: $**p = 0.002105$; $*p = 0.01138$; $\#\#p = 0.00003960$ $n = 5$ experiments; shown with SEM. **o** Representative images showing the proximity ligation assay between Flag-tagged TC10 (WT or 5× mut) and MYC-tagged Exo70 in MTLn3 cells. Cortactin fluorescence is also shown to denote the locations of invadopodia structures. The corresponding invadopodia locations are shown in the PLA images by dotted yellow circles. White bar = 10 μm. **p** Quantification of the PLA spots at invadopodia. Student's *t*-test, two-tail, $N = 3$ experiments; ns $p = 0.2541$, $**p = 0.002775$, $*p = 0.01599$, shown with SEM.

activity of the overexpressed WT TC10 biosensor depended on the adhesion status of cells, as trypsinization in order to suspend cells for measurements in cuvettes significantly reduced FRET (Fig. 4e). We used this feature of the WT TC10 biosensor to test for the specificity of activation response to a panel of GEFs including those targeting the RhoGTPases (Dbl- and DOCK-GEFs), RabGTPases, and Ras/RapGTPases. No significant increases in the TC10 biosensor activity were observed when the majority of the Dbl-homology GEFs were overexpressed together with the biosensor (Fig. 4f). Interestingly, the DOCK1/2/4 GEFs activated the biosensor (Fig. 4g), as did the RabGTPase-targeting Connecdenn1/3 and ST5 GEFs (Fig. 4h). Ras/RapGTPase-targeting GEFs were also able to activate TC10 (Fig. 4i). Some of the GEFs that activated the TC10 biosensor did so dependently on whether or not they were full-length or the truncated catalytic domain only, pointing to the importance of autoregulatory elements within the GEFs or through other scaffolding activity from domains within the truncated regions. The co-expression of RhoGTPase-targeting p50RhoGAP, p190RhoGAP, TcGAP, CdGAP, DLC-1, and the RabGTPase-targeting TBC1D10, but not RapGTPase-targeting Rap1GAP1 resulted in attenuation of FRET from the WT biosensor measured in attached cells, some dependent on the full length versus the truncated catalytic domain (Fig. 4j). These results point to the regulatory cross-talk between the different GTPase compartments, through overlapping targeting of TC10 by some GEFs and GAPs. To confirm that the expression of the TC10 biosensor did not result in aberrant overexpression artifacts in downstream signaling, we performed a competitive pull-down assay using the purified, exogenous binding domain. The activated TC10 biosensor only interacted with an exogenous effector when both biosensor binding domains within the biosensor were mutated (2XPBD: H83/86D), preventing interaction between activated TC10 and the GTPase binder motif within the biosensor backbone (Supplementary Fig. 8a). We then applied a synonymous codon modification[65], which prevents homologous recombination during transfection and transduction into cancer cells. When the TC10 biosensor was expressed in MTLn3 breast cancer cells, we observed an approximately 30% difference in whole-cell average TC10 activities between the constitutively active and dominant-negative versions of the TC10 biosensor (Supplementary Fig. 8b). The biosensor also responded to acute stimulation with serum and EGF following serum starvation (Supplementary Fig. 8c). We then overexpressed the biosensor FRET module without the GTPase, the full-length TC10 biosensor containing the WT TC10, and another different biosensor previously published which is also based on the same FRET detection module (biosensor for Rac3)[58] in MEFs to visualize the relative localization patterns in cells. Expressing only the FRET detection module resulted in a homogeneous distribution pattern within cells including the nucleus which *Aequoria victoria*-derived fluorescent proteins have been known to enter[66] (Supplementary Fig. 9a). The attachment of WT TC10 at the C-terminus of the FRET detection module produced localization patterns of the biosensor similar to the mCer3-TC10 (WT) expression (Supplementary Fig. 9b, c), whereas the expression of Rac3 biosensor showed different patterns, colocalizing strongly with focal adhesion-like structures, F-actin stress fibers, and often with visible nuclear localization (Supplementary Fig. 9d). These results indicate that the TC10 FRET biosensor localizes similar to the FP-tagged TC10 GTPase in cells and that the FRET detection module does not produce aberrant localization patterns of the biosensors when expressed. We also produced a near-infrared version of the TC10 FRET biosensor based on a previous design (Supplementary Fig. 10)[67], which behaved similar to the cyan-yellow version. Finally, the TC10 biosensor was stably transduced and integrated

into tet-OFF tTA-MTLn3 cells[68], under the control of a tet-inducible promoter to achieve expression control.

Using the TC10 FRET biosensor, we attempted to determine the dynamics of TC10 activity at and surrounding the invadopodia. We transfected cortactin-miRFP703 to serve as a marker of the invadopodia core and observed TC10 activity. The biosensor activities at invadopodia appeared to be highly dynamic and fluctuated markedly during live-cell imaging (Fig. 4k; Supplementary Movie 4), suggesting a stochastic behavior over time. We first reduced the complexity of the data in the time-

Fig. 4 TC10 activity at invadopodia is spatially regulated. a A schematic and a cartoon of the single-chain, genetically encoded FRET biosensor for TC10 GTPase, based on previous biosensor designs used to evaluate Rac/Cdc42-type GTPases[58, 60–62]. The FRET donor (cyan) and acceptor (yellow) were mCerulean1 and circularly permutated mVenus, respectively. **b** Representative, normalized fluorescence emission spectra of the constitutively activated (CA: Q75L) versus the dominant-negative (DN: T31N) versions of the TC10 biosensor upon excitation at 433 nm when overexpressed in HEK293T cells and measured in cell suspensions. Spectra were normalized to the peaks of the donor emission at 474 nm. **c** Fluorometric emission ratio of the TC10 biosensor overexpressed in HEK293T cells. WT biosensor expression and the Q75L and G26V CA mutant biosensors showed high emission ratios. The DN biosensor, CA biosensors with GTPase binding-deficient mutations in both PBD domains (Q75L-H83/86D), and effector binding mutants (T49A, Y54C) showed low emission ratios. Student's t-test, two-tail analysis: ns $p = 0.06587$ for Q75L, $p = 0.3810$ for G26V; $^{**}p = 1.544 \times 10^{-6}$ for T31N, $p = 0.001531$ for Q75L-H83/86D, $p = 0.0001294$ for T49A, and $p = 0.0001279$ for Y54C, all compared to the WT (first bar); $n = 7$ experiments for WT, 4 experiments for all other conditions, all shown with SEM. **d** The co-expression of the DN mutant (T31N) of TC10 attenuates the WT TC10 biosensor FRET response. Student's *t*-test, two-tail analysis: $^{*}p = 0.01078444$; $^{**}p = 0.0002401$; 3.008×10^{-6}; 3.314×10^{-7}; 7.600×10^{-8}; $N = 18$ for the WT-BS; $N = 3$ for the DN titrations, shown with SEM. **e** The cell detachment by trypsinization reduces the WT TC10 biosensor FRET to baseline. Student's t-test, two-tail analysis: $^{**}p = 3.161 \times 10^{-5}$; $N = 4$ experiments, shown with SEM. **f** The co-expression of GEFs targeting cytoskeletal Rho GTPases, together with WT TC10 biosensor measured in detached cells. Student's *t*-test, two-tail analysis: ns (in the order left to right) $p = 0.961607$; 0.126906; 0.855333; 0.092082; 0.260474; 0.384857; 0.227471; 0.218374; 0.380141; 0.161537; 0.093242; 0.375213; 0.98228; and 0.494; ** (in the order left to right) $p = 0.001237$; 0.000457; and 0.007204; and $^{*}p = 0.028181$; $N = 13$ for WT-BS, $N = 3$ for the GEF co-expression, shown with SEM. **g** The co-expression of Dock GEFs, together with WT TC10 biosensor measured in detached cells. Student's *t*-test, two-tail analysis: ** (in the order left to right) $p = 0.001105$; 6.971×10^{-5}; 1.268×10^{-5}; and 8.575×10^{-6}; and $^{*}p = 0.01056$; $N = 13$ for WT-BS, $N = 4$ for the Dock1-cat; $N = 3$ for the other Dock GEFs, shown with SEM. **h** The co-expression of GEFs targeting Rab GTPases, together with WT TC10 biosensor measured in detached cells. Student's *t*-test, two-tail analysis: ** (in the order left to right) $p = 3.888 \times 10^{-5}$; 3.216×10^{-5}; 3.232×10^{-8}; 2.540×10^{-6}; and 6.356×10^{-8}; ns $p = 0.06056$; $N = 13$ for WT-BS, $N = 3$ for GEF co-expression, shown with SEM. **i** The co-expression of GEFs targeting Rap/Ras GTPases, together with WT TC10 biosensor measured in detached cells. Student's *t*-test, two-tail analysis: ns (in the order left to right) $p = 0.05669$; 0.5828; 0.2413; 0.1330; and 0.05510; ** (in the order left to right) $p = 3.297 \times 10^{-7}$; 0.0004357; 0.001887; 0.0005196; 0.007521; 0.003384; 0.005243; 0.0006635; and 0.0004461; $^{*}p = 0.04514$; $N = 13$ for WT-BS, $N = 4$ for GEF co-expression, shown with SEM. **j** The co-expression of GAPs together with WT TC10 biosensor was measured in attached cells. Student's *t*-test, two-tail analysis: ** (in the order left to right) $p = 1.070 \times 10^{-7}$; 0.003775; 1.709×10^{-5}; 5.050×10^{-5}; and 0.001420; ns (in the order left to right) $p = 0.4286$; 0.06161; and 0.3204; $^{*}p = 0.03834$; $N = 11$ for WT-BS; $N = 5$ for TcGAP (full and cat), CdGAP (full and cat), TBC1D10, and DLC1; $N = 4$ for p50 RhoGAP and p190RhoGAP; and $N = 3$ for Rap1GAP1; shown with SEM. **k** Representative, dynamic localization patterns of TC10 activity at and surrounding the invadopodium core (denoted by cortactin fluorescence). The time-lapse sequence panel is shown with minutes': seconds", where the start of imaging being 00:00 (also shown in Supplementary Movie 4). **l** The line scan analysis of the intensity distributions across invadopodia showing normalized TC10 activity integrated over time, averaged, and plotted against the matching averaged cortactin intensity distributions. The blue-shaded regions indicate significant differences ($p < 0.05$; Student's *t*-test, one-tail; $n = 33$ invadopodia from 19 cells over 7 experiments; for *p*-value distributions see Supplementary Data 1) in TC10 activity intensity compared with the invadopodia core center at 0.0 μm. Line scans were normalized to the local maxima of TC10 activity at the ring-like region surrounding the invadopodia core defined by the cortactin spot, and dilating such a region of interest by approximately one diameter distance (shown with dotted concentric circles in (**k**). The cortactin intensity was normalized at the center position, taken as the maximal intensity location along with the line scans. Averaged line scans (solid lines) are plotted with corresponding SEM (dashed lines). **m** Autocorrelation functions showing fluctuations in TC10 activity in the invadopodia core (red) versus the ring-like region (blue) around the invadopodia core. The gray lines (solid: core; dashed: ring) indicate the 95% confidence intervals around the mean. $N = 29$ invadopodia core and ring measurements, from 19 different cells, in 8 experiments.

domain by integrating the TC10 activities over time in steady-state invadopodia, similar to a previous analysis performed for a different class of Rho GTPase[59]. We measured and averaged the line scans across invadopodia and determined that the center of the invadopodium core showed a significant reduction in time-integrated TC10 activity compared with the regions surrounding the invadopodium core (Fig. 4l). This observation indicated a spatially ordered distribution of TC10 activity underlying the apparent stochastic fluctuation. A similar observation was made in MDA-MB 231 cells (Supplementary Fig. 11). To further quantify the TC10 activity fluctuation, we defined two regions by generating a binary mask, with one region based on the cortactin core (core) and the second region defined by dilating the core mask by 30 pixels and subtracting the core to form an annulus (ring). The live-cell biosensor measurements were analyzed by autocorrelation to extract the characteristic periodicity of fluctuation[58,69,70] at these two regions. We observed essentially no periodic fluctuations in TC10 activity for either of the regions, as characterized by the lack of repeated, oscillatory crossings of the zero axis in the autocorrelation functions[69] (Fig. 4m). These findings indicated that the TC10 activity dynamics in the wild-type, steady-state invadopodia are stochastic. Importantly, the time-integrated activity of TC10 is attenuated significantly in the core, indicating a mechanism through which a core-localized GAP may regulate TC10 GTP-hydrolysis at the invadopodia core.

p190RhoGAP impacts invadopodia function by targeting TC10. To identify the regulator of TC10 function at invadopodia, we focused on p190RhoGAP (*Arhgap35*), a well-known, integrin-adhesion-associated regulator of RhoGTPases, which binds cortactin within the invadopodia core during invadopodia precursor formation and is present within the core of invadopodia at steady state[19]. Traditionally, p190RhoGAP targets Rac and Rho GTPase isoforms and contains: an N-terminal GTPase-binding domain; four FF domains involved in binding transcription factors; a protrusion localization domain that binds cellular cortactin or Rnd3 GTPase; a p120RasGAP binding site; a polybasic region; and a C-terminal consensus GAP domain that can switch specificity between Rac-GTP or Rho-GTP[71,72]. p190RhoGAP has been associated with the regulation of TC10 activity in a number of systems, including the leading edge of HeLa cells and neurite extensions[35,73]. In melanoma, tyrosine phosphorylation and the activation of p190RhoGAP at invadopodia in response to laminin peptide depends on the activation of β1 integrins[74]; in breast cancer, invadopodia precursor β1 integrins are activated within 3–5 min after EGF stimulation in a Rac3 GTPase-dependent manner[42,58]. β1 integrin recruits the non-receptor tyrosine kinase Arg (Ableson-related gene, also known as Abl2) and stimulates the Arg-dependent phosphorylation of p190RhoGAP at the leading edge of fibroblasts; however, whether this occurs in breast cancer cell invadopodia has not yet been elucidated.

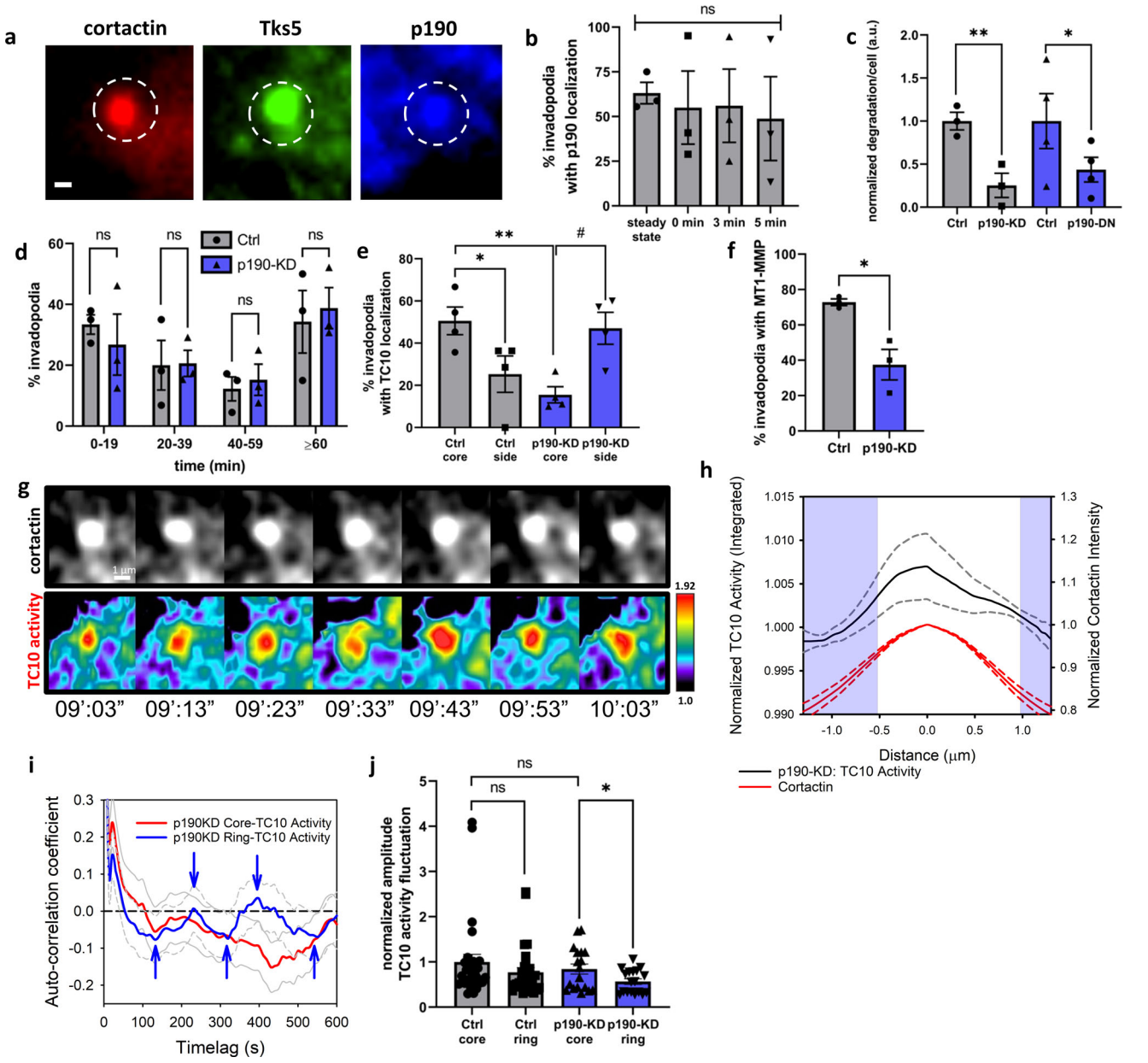

Steady-state and EGF-stimulated invadopodia precursor assays demonstrated that p190RhoGAP is a resident protein of the invadopodia core (Fig. 5a, b), and p190RhoGAP depletion (Supplementary Fig. 12) phenocopied the ECM degradation deficiency observed with TC10 depletion (Fig. 5c and Supplementary Fig. 13a, b). The overexpression of a dominant-negative version of p190RhoGAP, which lacks the ability to activate GTP hydrolysis by Rho GTPases, also strongly inhibited ECM degradation (Fig. 5c). Moreover, invadopodia lifetimes were not impacted by p190RhoGAP depletion (Fig. 5d), which suggested that p190RhoGAP is associated with the functional aspects of invadopodia, similar to TC10. p190RhoGAP depletion was associated with a reduction in the TC10 fraction observed in the invadopodia core, accompanied by an increase in the proportion of TC10 observed in the lateral aspects of invadopodia (Fig. 5e), which suggested that the flux of TC10 through the ring-like region and into the invadopodia core was significantly attenuated by p190RhoGAP depletion. In line with our hypothesis that TC10 activity might be affected by perturbations in p190RhoGAP activity, p190RhoGAP depletion also impacted the exocytic surface presentation of MT1-MMP in a manner similar to that observed for TC10 depletion (Fig. 5f). These findings indicated that p190RhoGAP plays an important role in the regulation of invasive functions associated with invadopodia.

Next, we wished to determine the functional impacts of p190RhoGAP on TC10 activity at invadopodia. We used our FRET biosensor to monitor changes in TC10 activity following p190RhoGAP depletion at invadopodia. Live-cell imaging of TC10 activity in p190RhoGAP-depleted cells revealed strong fluctuations in the activity patterns at and surrounding the invadopodia (Fig. 5g; Supplementary Movie 5). We integrated the TC10 activity over time at invadopodia and performed a line scan analysis, which showed that the time-integrated activity of TC10 was significantly elevated within the invadopodia core in cells with p190RhoGAP depletion (Fig. 5h). To characterize the temporal fluctuations of TC10 activity at invadopodia under p190RhoGAP depletion conditions, we used the autocorrelation analysis[69]. We found that the core-associated TC10 activity dynamics were essentially stochastic and lacked periodicity, similar to the wild-type conditions (Figs. 5i and 4m). We found

Fig. 5 p190RhoGAP impacts invadopodia function by targeting TC10. a Representative, immunostaining of endogenous p190RhoGAP at the invadopodia core, in MTLn3 cells. White bar = 1 μm. **b** The percentage of invadopodia with p190RhoGAP localization in MTLn3 cells, following starvation and EGF stimulation (5 nM) for the indicated times. The steady-state percentage of invadopodia with p190RhoGAP localization in MTLn3 cells in serum is also shown. Student's *t*-test, two-tail analysis: ns $p = 0.7220$, steady-state versus 0 min; $p = 0.9730$, 0 min versus 3 min; $p = 0.8520$, 0 min vs. 5 min; $n = 3$ experiments; shown with SEM. **c** Matrix degradation from MTLn3 cells transfected with control siRNA (Ctrl, gray) or siRNA against p190RhoGAP (KD, gray), and the overexpression of a catalytically dead p190RhoGAP dominant-negative mutant (DN, blue). Results are normalized to the Ctrl. p190RhoGAP depletion characterization and efficiency evaluations are shown in Supplementary Figure 12. Student's *t*-test, two-tail analysis: $^{**}p = 0.006336$; $n = 3$ experiments; shown with SEM; $^{*}p = 0.04141$; $n = 4$ experiments; shown with SEM. **d** Invadopodia lifetime assay in MTLn3 cells transfected with Ctrl versus p190RhoGAP siRNA. Student's *t*-test, two-tail analysis: ns, $p = 0.5646$ for 0–19 min; $p = 0.9495$ for 20–39 min; $p = 0.6673$ for 40-59 min; $p = 0.7356$ for >60 min; $n = 3$ experiments, shown with SEM. **e** The localization of TC10 in MTLn3 cells transfected with Ctrl or p190RhoGAP siRNA. Student's *t*-test, one-tail analysis: $^{**}p = 0.005126$; $n = 4$ experiments; shown with SEM; Student's *t*-test, paired one-tail analysis: $^{*}p = 0.033138$; $\#p = 0.03791$; $n = 4$ experiments; shown with SEM. **f** The percentage of invadopodia with extracellular, endogenous MT1-MMP localization from among 231 cells, transfected with either Ctrl or p190RhoGAP siRNA. Student's *t*-test, paired one-tail analysis: $^{*}p = 0.02492$; $n = 3$ experiments; shown with SEM. **g** Representative example images of TC10 biosensor activity at an invadopodium in MTLn3 cells transfected with p190RhoGAP siRNA. The invadopodium is denoted by the cortactin fluorescence signal. The time-lapse sequence panel is shown with minutes': seconds", where the start of imaging being 00:00 (also shown in Supplementary Movie 5). **h** The line scan analysis of the intensity distributions across invadopodia for TC10 activity integrated over time, showing the p190RhoGAP-depleted condition, averaged and plotted together with the normalized averaged cortactin trace. The blue-shaded regions indicate significant ($p < 0.05$; Student's *t*-test, one-tailed; $n = 25$ invadopodia from 12 cells over 3 experiments; For *p*-value distributions, see Supplementary Data 1) differences from the TC10 activity intensity at the center of the invadopodia core at 0.0 μm. TC10 activity line scans were normalized to the position at the ring-like region surrounding the invadopodia core, as determined and shown in Fig. 4k. The cortactin intensity was normalized at the center position, taken as the maximal intensity location along with the line scans. Averaged line scans (solid lines) are plotted with corresponding SEM (dashed lines). **i** Autocorrelation functions for the fluctuation of TC10 activity when p190RhoGAP is depleted in the invadopodium core (red) versus the ring-like region (blue) around the invadopodium core. The gray lines (solid: core; dashed: ring) indicate the 95% confidence intervals around the mean. The autocorrelation function in the core of invadopodia does not inflect after the first zero-crossing (no apparent periodicity). The autocorrelation function in the ring region has repeating inflection patterns that cross zero several times at an apparent, characteristic periodicity (inflection points are indicated with blue arrows) of approximately 229 ± 28 s. $N = 18$ invadopodia core and ring measurements from 10 different cells in 3 experiments. **j** The absolute values of the amplitude of fluctuation in the TC10 biosensor activity in the core versus the ring-like region around the invadopodium core. The data are normalized to the core fluctuation amplitudes in the WT condition (first bar). Student's t-test, two-tail analysis: ns $p = 0.2546$ (WT core versus WT ring), ns $p = 0.4415$ (WT core versus p190KD core), $^{*}p = 0.03771$ (p190KD core versus p190KD ring); $n = 29$ invadopodia core and ring measurements for WT, from 19 different cells, in 8 experiments, and $n = 18$ invadopodia core and ring measurements for p190KD from 10 different cells in 3 experiments; shown with SEM.

that p190RhoGAP depletion produced a fluctuation, with a modest but measurable periodicity of oscillations in TC10 activity in the ring-like region surrounding the core (Fig. 5i). The characteristic periodicity observed within the ring-like region of invadopodia was approximately 229 ± 28 s, which was within a similar order of magnitude as previously determined invadopodium core protein fluctuation rates, including those for cortactin and neural Wiskott-Aldrich syndrome protein (N-WASP)[75]. These observations suggested a hypothesis in which the transient, bulk flux of TC10 activity simply moves through the ring-like region surrounding the invadopodia core in the absence of GTP hydrolysis when p190RhoGAP is depleted (Supplementary Fig. 13c). The absolute value of the fluctuation amplitude was significantly reduced in the ring-like region compared with that in the core when p190RhoGAP was depleted (Fig. 5j), supporting the hypothesis that p190RhoGAP depletion resulted in reduced degrees of freedom. This observation is consistent with the hypothesis that p190RhoGAP regulates the ability of TC10 to hydrolyze GTP as it transits from the ring-like region into the invadopodia core, where p190RhoGAP primarily resides.

In addition to targeting TC10, RhoC GTPase activity is also directly impacted by p190RhoGAP[55,59,76]. Previously, the inactivation of RhoC was shown to increase ECM degradation at invadopodia via a mechanism associated with changes to the invadopodia structural cohesion through the RhoC-Rho-kinase 1 (ROCK)-LIM kinase (LimK)-cofilin-phosphorylation pathway[59]. p190RhoGAP depletion would, therefore, be expected to cause the overactivation of RhoC[76]. We generated a fast-cycling, constitutively activated RhoC (F30L) that contained a set of GAP-binding deficiency mutations (E93H and N94H)[77]. The overexpression of this mutant RhoC would allow the effects of p190RhoGAP depletion to be mimicked for RhoC without affecting the ability of native p190RhoGAP to target other GTPases including TC10. The overexpression of this RhoC mutant impacted ECM degradation but had no significant effects on the total number of steady-state invadopodia or the relative MT1-MMP localization at invadopodia (Supplementary Fig. 14a–c). However, as expected, based on the structural effects of RhoC on invadopodia, we observed a shift in the invadopodia lifetimes, favoring structures with faster turnover rates and reducing those with longer lifetimes (Supplementary Fig. 14d). An increase in the population of invadopodia that turnover rapidly is associated with structural instability, which impacts invadopodia maturation and reduces ECM degradation. Thus, RhoC activation affects ECM degradation, likely through structural effects rather than vesicular targeting or fusion defects. These observations indicate the divergent roles of TC10- and RhoC-driven pathways at invadopodia that are simultaneously regulated by a single upstream regulator p190RhoGAP.

Tyrosine phosphorylation of p190RhoGAP is required for ECM degradation. The phosphorylation of p190RhoGAP by the non-receptor tyrosine kinase Arg promotes the binding of p190RhoGAP to p120RasGAP and initiates the recruitment of the p190:120-complex to the cell periphery, where the GAP activity of p190RhoGAP for RhoGTPases is potentiated[78,79]. Arg is activated by β1 integrin-binding during invadopodia maturation[42]. Arg phosphorylates p190RhoGAP at Y1105, in the RasGAP-binding region, and Y1087, which stabilizes the interaction between p190RhoGAP and p120RasGAP[78]. Therefore, we determined the phosphorylation status at Y1105 of p190RhoGAP at invadopodia and examined how phosphorylation activity affected the p190RhoGAP-mediated regulation of invadopodia functions. Approximately 90% of steady-state invadopodia

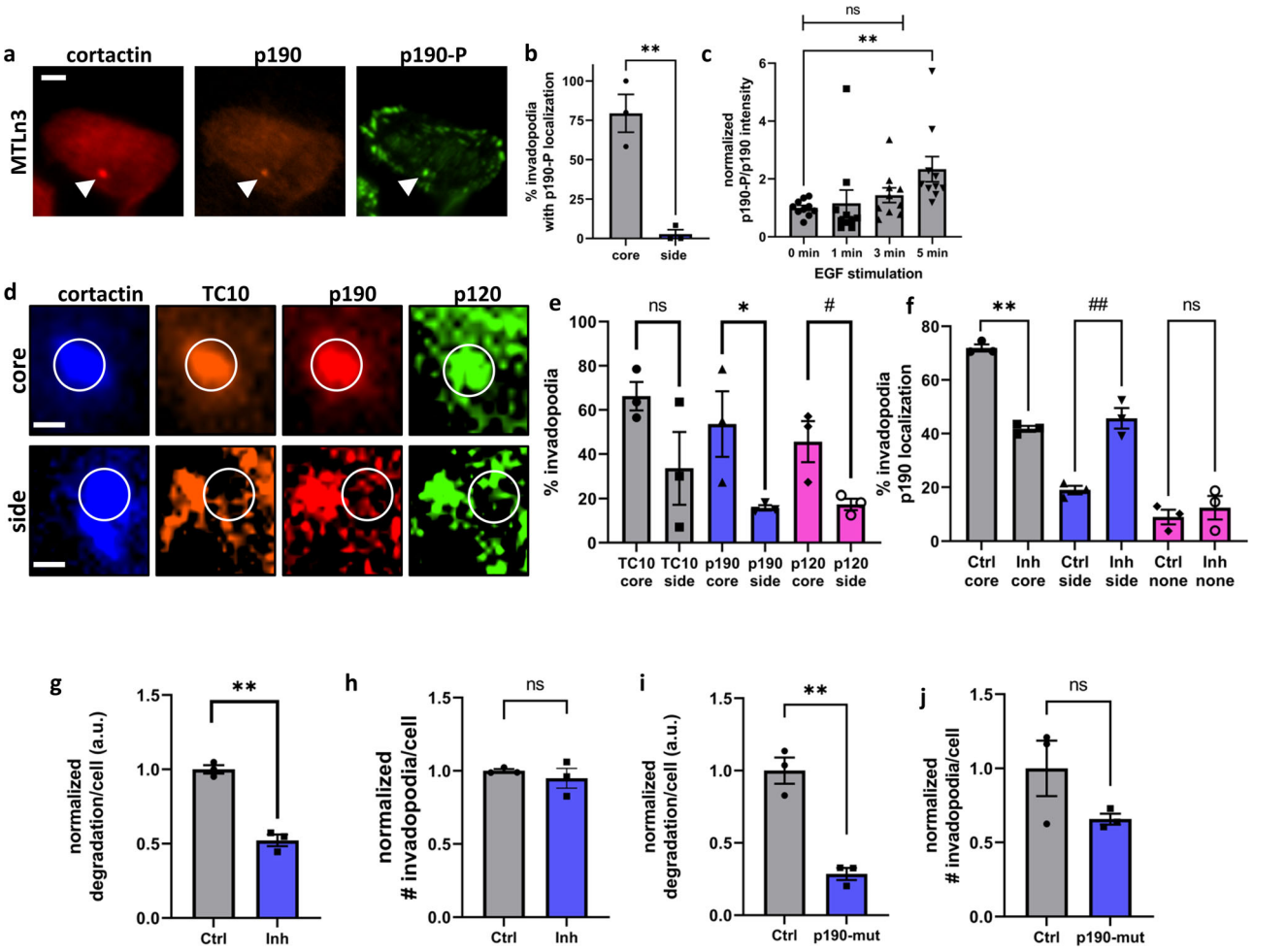

Fig. 6 Tyrosine phosphorylation of p190RhoGAP is required for matrix degradation. a Representative, immunostaining for endogenous p190RhoGAP and Y1105-phosphorylated p190RhoGAP, co-expressed with mtagRFP-T-cortactin as an invadopodia marker. White bar = 5 µm. **b** Quantification of the percentage of invadopodia that were positive for phosphorylated p190RhoGAP colocalization. Student's t-test, two-tail analysis: $^{**}p = 0.0001518$; $n = 3$ experiments, shown with SEM. **c** The ratio of phosphorylated p190RhoGAP to total p190RhoGAP at invadopodia in MTLn3 cells during invadopodia precursor formation, induced by 5 nM EGF treatment following starvation for the indicated times. Results are normalized to the ratio at 0 min. Student's *t*-test, two-tail analysis: ns $p = 0.742460426$ for 0–1 min; $p = 0.120533868$ for 0–3 min; and $^{**}p = 0.007470$ for 0–5 min; $n = 3$ experiments, shown with SEM. **d** Representative, immunostaining of endogenous p190RhoGAP and p120RasGAP at invadopodia, shown together with the co-expression of fluorescent protein-tagged WT TC10 and cortactin. White bar = 1 µm. **e** Quantification of endogenous p190RhoGAP and p120RasGAP localization at either the core or the side of invadopodia. Student's *t*-test, two-tail analysis: ns $p = 0.3618$ for TC10 core vs. side; $^{*}p = 0.01146$ for p190 core vs. side; $\#p = 0.04271$ for p120 core vs. side; $n = 3$ experiments, shown with SEM. **f** Quantification of the change in p190RhoGAP localization upon overexpression of the p190:p120 competitive binding inhibitor. Student's t-test, two-tail analysis, $^{**}p = 0.00006365$; $\#\#p = 0.002991$; ns $p = 0.5417$; $n = 3$ experiments, shown with SEM. **g** Quantification of matrix degradation by MTLn3 cells when the p190:p120 competitive binding inhibitor was overexpressed. Results are normalized to the Ctrl where only the fluorescent protein was overexpressed. Student's *t*-test, one-tail analysis: $^{**}p = 0.0002822$; $n = 3$ experiments, shown with SEM. **h** The number of steady-state invadopodia in MTLn3 cells when the p190:p120 competitive binding inhibitor was overexpressed. Results are normalized to the Ctrl where only the fluorescent protein was overexpressed. Student's *t*-test, two-tail analysis: ns $p = 0.5016$; $n = 3$ experiments, shown with SEM. **i** Quantification of the matrix degradation by MTLn3 cells when a Y1105/1087 phosphorylation-deficient mutant version of p190RhoGAP was overexpressed. Results are normalized to the Ctrl where only the fluorescent protein was overexpressed. Student's t-test, one-tail analysis: $^{**}p = 0.001009$; $n = 3$ experiments, shown with SEM. **j** The number of steady-state invadopodia in MTLn3 cells when a Y1105/1087 phosphorylation-deficient mutant version of p190RhoGAP was overexpressed. Results are normalized to the Ctrl where only the fluorescent protein was overexpressed. Student's t-test, two-tail analysis: ns $p = 0.1475$; $n = 3$ experiments, shown with SEM.

contained Y1105-phosphorylated p190RhoGAP, which was found both in the core compartment and occasionally on the lateral sides of invadopodia (Fig. 6a, b), which agrees with a previous study that only the active, phosphorylated form of p190RhoGAP was recruited to the plasma membrane to act on RhoGTPases[78,79]. The phosphorylation of p190RhoGAP at Y1105 is time-dependent following EGF stimulation to induce the synchronous formation of invadopodia precursors (Fig. 6c), mirroring the previously described Arg-mediated phosphorylation events at the invadopodium core following EGF stimulation[80]. In line with the tyrosine-phosphorylated status of p190RhoGAP, we observed a strong colocalization between p120RasGAP, p190RhoGAP, and TC10 at invadopodia, either on the side of the invadopodia or in the core, overlapping with the cortactin signal (Fig. 6d, e). The colocalization of p190RhoGAP at the invadopodia core was significantly altered by the expression of a competitive inhibitor of p190:120-binding[78,79], shifting to a lateral localization pattern (Fig. 6f). The

presence of this competitive inhibitor also reduced ECM degradation (Fig. 6g) without impacting the number of steady-state invadopodia (Fig. 6h). Phosphorylation-deficient p190RhoGAP point mutations, in which the two tyrosines were replaced with phenylalanines (Y1105F and Y1087F), strongly impacted ECM degradation, similar to the effects observed in response to TC10 and p190RhoGAP depletion and the overexpression of the p190:120 competitive binding inhibitor (Fig. 6i). However, these p190RhoGAP point mutations only affected the functional aspects of invadopodia without affecting the number of steady-state invadopodia (Fig. 6j). These observations indicated that p190RhoGAP is targeted to the invadopodia core through tyrosine phosphorylation, which promoted p120RasGAP binding and regulated ECM degradation.

TC10 is required for cancer cell metastasis in vivo. We attempted to determine the functional relevance of TC10 signaling for the process of breast cancer cell invasion and metastasis. We first investigated the ability of tumor cells to invade through the ECM using an in vitro invasion assay, in which cultured tumor cells respond to serum stimulation by migrating through a Matrigel-coated filter[28]. Compared with the control siRNA-treated condition, TC10 depletion significantly impacted the ability of MTLn3 cells to invade through Matrigel-coated filters in an in vitro invasion assay (Fig. 7a), which was expected due to the reduced ECM degradation capacity and the reduced MT1-MMP presentation at invadopodia. Moreover, p190RhoGAP depletion in MTLn3 cells also significantly attenuated the ability of these cells to invade, phenocopying TC10 depletion (Fig. 7b). To examine whether TC10 is required for breast tumor metastasis in a mouse model, we generated a clustered regularly interspaced short palindromic repeat (CRISPR)/CRISPR-associated protein 9 (Cas9)-driven TC10 knockout cell line in MTLn3 cells that stably express EGFP. We chose the CRISPR/Cas9 knockout cell population expressing single-guide RNA (sgRNA) #4, which showed the strongest initial TC10 knockout efficiency in a stable cell population (Fig. 7c). We subsequently reanalyzed for TC10 expression levels following a cycle of freeze/thaw and maintenance in cell culture for several passages. We observed a ramping up of TC10 re-expression, stabilizing to approximately 50% levels in this population over time, which is similar to our siRNA-mediated TC10 depletion levels (Fig. 7d, e). We therefore considered these cells as CRISPR/Cas9-TC10-knockdown populations, with stable genetic depletion of TC10. CRISPR-TC10 cells showed significant ECM degradation defects (Fig. 7f) but no changes in the total number of steady-state invadopodia, similar to the effects observed for siRNA-mediated TC10 depletion (Fig. 7g). ECM degradation deficiencies in the CRISPR-TC10 cells could be fully rescued by the overexpression of WT TC10 (Fig. 7h). We orthotopically injected the CRISPR-TC10 cells into the mammary fat pads of 6–8-week-old female severe combined immunodeficient (SCID) mice and examined lung metastasis after the primary tumor reached 1 cm in diameter. Lung metastasis was significantly impacted in mice bearing CRISPR-TC10 MTLn3 tumors compared with mice bearing non-targeting control tumors (Fig. 7i, j; additional example fields of view shown in Supplementary Fig. 15). Together, these results indicate that TC10 functionally impacts breast tumor dissemination and metastasis.

Discussion

In this study, we demonstrated a role for TC10 GTPase, a close paralog of Cdc42, at tumor invadopodia during breast cancer invasion and metastasis. We designed these studies to test our hypothesis that an important, previously unidentified GTPase might regulate the invadopodia surface presentation of MT1-MMP enzymes, which are necessary for ECM degradation during tumor invasion. We set out to address this question by developing a FRET biosensor for TC10, based on monomeric, single-chain, and genetically encoded design, with approximately 10-fold greater response dynamic range than a previous generation FRET biosensor for TC10 in the field[35]. Our results present a model in which TC10 regulates MT1-MMP-containing vesicular fusion at the invadopodia membrane, controlled by the activity modulation of TC10 by the upstream regulator p190RhoGAP (*Arhgap35*) at invadopodia (Fig. 7k). Our findings demonstrate that TC10 plays an important role during breast cancer invasion and metastasis through the control of ECM degradative functions at invadopodia structures.

TC10 depletion resulted in significant impacts on the ability of tumor cells to degrade the ECM, associated with a decrease in the surface exposure of MT1-MMP at invadopodia. Because the overall number of steady-state invadopodia and invadopodia lifetimes were not significantly impacted by TC10 perturbations, we conclude that TC10 primarily plays a functional role at invadopodia, without impacting the control of the turnover or the formation rates of invadopodia. This finding is in stark contrast to the role played by the canonical and highly related GTPase, Cdc42, at invadopodia: The activation of Cdc42 by an upstream GEF, Vav1, has been shown to be critical for the initial formation of invadopodia precursors[81,82]. We also observed the transient but persistent activation of Cdc42 within the nascent core of invadopodia precursor structures during the assembly of the cortactin core (Supplementary Fig. 16). Our observations indicated that these close paralog GTPases play divergent roles at invadopodia structures during invadopodia assembly and function.

Interestingly, the depletion of TC10 in MTLn3 cells led to a reduction in the density of the cortactin core of an invadopodium, without affecting other dynamic metrics. Previous findings from our work and from others, have pointed to the mechanism by which the stability of invadopodia structures play an important role in their maturation[42,58,59,61,83]. Those studies generally focused on the regulation of adhesion and actin-polymerization, which are critical for an efficient invadopodium maturation process, evidenced by altered dynamic metrics including the turnover or the formation rates[42,58,59,61,83]. Here, TC10 depletion points to changes in cortactin structural density that does not affect the overall invadopodia size, the turnover, or the formation rates. Therefore, it is possible that our results also demonstrate a structural role through an impaired delivery of components to the invadopodia core, including cortactin, which may ultimately destabilize these structures and change the efficiency of invasion during metastasis. This aspect could be particularly important for invadopodium-associated force generation, which also regulates cell invasion through varying ECM density, stiffness, and malleability[26,84–89].

p190RhoGAP has been documented to primarily target Rac and Rho GTPases[90]. We previously localized p190RhoGAP at both the leading edge and the core of invadopodia in breast cancer cells[59,76], likely due to binding with cortactin via its protrusion localization domain[43]. In these previous studies, we showed that p190RhoGAP targeted another class of RhoGTPase, RhoC, to control actin polymerization both at the leading edge and within the core of invadopodia[59,76]. In our present work, we showed that p190RhoGAP also targets TC10 at invadopodia to regulate TC10 activity, which ultimately affects the surface presentation of MT1-MMP and ECM degradation. Moreover, we previously showed that Rac1 activity was attenuated within the invadopodia core and that the subsequent activation of Rac1 was critical for the regulation of invadopodia structural turnover[61]. Although we did not identify a specific GAP involved in Rac1

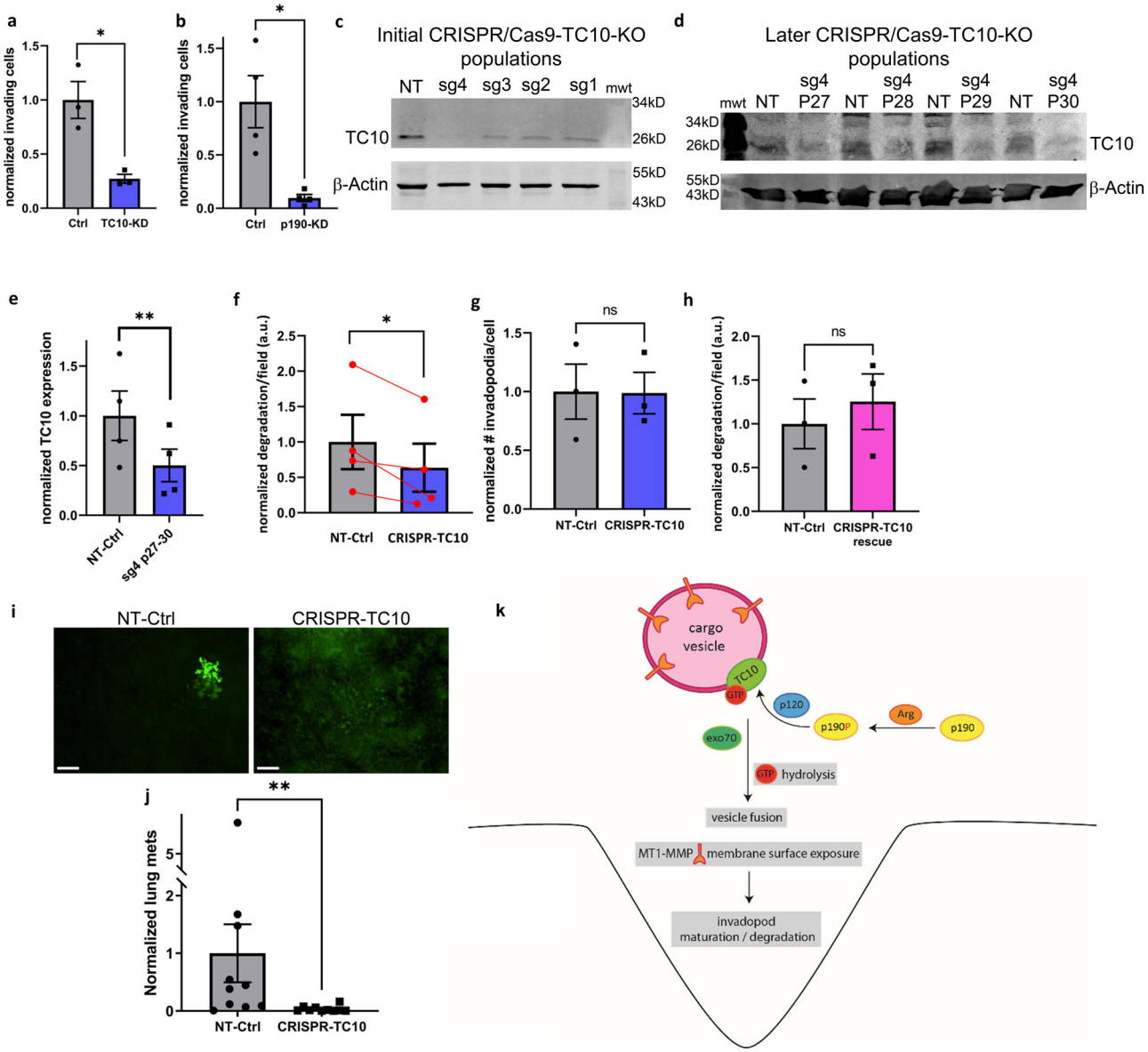

Fig. 7 TC10 is required for cancer cell metastasis in vivo. a The normalized number of invading cells in an in vitro invasion assay for MTLn3 cells transfected with Ctrl or TC10 siRNA. Student's *t*-test, one-tail pair-wise analysis, $^{*}p = 0.03928$, $n = 6$ experiments. Error bars represent the SEM. **b** The normalized number of invading cells in the in vitro invasion assay using MTLn3 cells transfected with Ctrl or p190RhoGAP siRNA. Student's t-test, one-tail pair-wise analysis: $^{*}p = 0.02312$; $n = 3$ experiments; shown with SEM. **c** Initial characterization of the CRISPR/cas9 TC10-knockout in MTLn3 cells using 4 different sgRNA designs, immediately after establishing stable populations (cell passage number 23). Full-sized western blots are shown in Supplementary Figure 19. **d** Characterization of sg4-TC10-KO population, following a single freeze/thaw cycle and subsequent passages in culture (passage numbers 27–30). Full-sized western blots are shown in Supplementary Figure 19. **e** Quantification of data shown in (**d**), averaged over passages 27 through 30. Student's *t*-test, one-tail analysis: $^{**}p = 0.008150$; $n = 4$ experiments, shown with SEM. **f** The matrix degradation by a CRISPR-TC10 MTLn3 cell population using sgRNA4. Results are normalized to the NT Ctrl degradation. Student's *t*-test, one-tail pair-wise analysis, $^{*}p = 0.03370$, $n = 4$ experiments. Error bars represent the SEM. **g** The number of steady-state invadopodia per cell in MTLn3 cells, with or without CRISPR-TC10 depletion. Results are normalized to the NT-Ctrl. Student's *t*-test, two-tail pair-wise analysis, ns $p = 0.9438$, $n = 4$ experiments. Error bars represent the SEM. **h** Functional rescue of matrix degradation by the overexpression of WT TC10 in CRISPR-TC10 MTLn3 cells. Results are normalized to the NT-Ctrl degradation. Student's *t*-test, one-tail pair-wise analysis, ns $p = 0.1737$, $n = 3$ experiments. Error bars represent the SEM. **i** Representative fields of views of the lung surface metastases of the Ctrl non-targeting or CRISPR-TC10 MTLn3 cells in the spontaneous metastasis assay, visualized using the co-transduced EGFP (additional examples are shown in Supplementary Fig. 15). White bars, 100 μm. **j** Quantification of (**i**). Results are normalized to the NT-Ctrl. $N = 12$ mice for Ctr and $n = 10$ for CRISPR-TC10. $^{**}p = 0.001380$ (Mann–Whitney U test, two-tail analysis). Error bars represent the SEM. **k** A schematic model showing the pathways regulated through TC10 modulation impacting breast cancer invasion and metastasis.

regulation in that study, the over-activation of Rac1 reduced the total number of invadopodia, whereas the depletion of p190RhoGAP in the present study did not change the total number of steady-state invadopodia or affect invadopodia life-times compared with control conditions. These observations suggest that a different set of signaling pathways are likely responsible for regulating Rac1 activity at invadopodia, separate from the p190RhoGAP pathway. RhoGAPs have been shown to be highly promiscuous, interacting with many GTPases[91]; therefore, the multi-specificity of p190RhoGAP at invadopodia is

likely to coordinate the signaling regulation of a number of RhoGTPases, including RhoC and TC10 but not Rac1.

Interestingly, the depletion of p190RhoGAP led to an accumulation of TC10 at the lateral side of invadopodia, while the fraction of TC10 occupying the core of invadopodia was significantly reduced. This observation suggests that the flux of TC10-containing vesicles into the invadopodia core region is impacted when p190RhoGAP is depleted. Corroborating this observation, a complete shutdown of vesicular flux has been previously observed when another GTPase important for the regulation of vesicular trafficking, (Arf6) was perturbed[58,92]. Here, the GTP-hydrolysis by TC10 was perturbed through the depletion of p190RhoGAP. This perturbation of the p190-TC10 signaling node likely prevented the exocytic fusion of the vesicles at the plasma membrane of the invadopodia core and significantly attenuated the flux and coalescence of the vesicles containing TC10 into the invadopodia core compartment. Importantly, those TC10 molecules that were still able to transport into the invadopodia core compartment when p190RhoGAP was depleted, showed significantly elevated activity, pointing to the lack of p190RhoGAP-action on that population of TC10.

During the p190RhoGAP activation[93], the non-receptor tyrosine kinase Arg phosphorylates p190RhoGAP at two important tyrosines (Y1105 and Y1087) in a β1 integrin activation-dependent manner[78]. The phosphorylation of these two sites is required for the formation of a complex between p190RhoGAP and p120RasGAP, which controls the localization and GAP activity of p190RhoGAP toward RhoGTPases during cell adhesion[78,94,95]. In line with the important role played by p120RasGAP binding on the control of p190RhoGAP localization and function, p120RasGAP depletion also resulted in reduced ECM degradation by invadopodia (Supplementary Fig. 17). However, we also noted a small but significant reduction in the total number of invadopodia when p120RasGAP was depleted (Supplementary Fig. 17). This observation indicates that p120RasGAP also plays a role in invadopodia assembly or the maintenance of structural components, possibly associated with its documented role during β1/2 integrin recycling[96]. Changes in integrin recycling mechanisms could alter the availability of functional integrins at the cell surface, which potentially affects invadopodia stability and turnover. Our findings underscore the importance of the localization and functional mechanisms of the p190:p120 GAP-signaling complex at the invadopodia core, which targets GTPases, including TC10, to regulate invadopodia functions.

The functional consequences of the regulation of TC10 activity and the associated effects on ECM degradation, cell invasion, and metastasis were underscored by our findings from the in vitro invasion and in vivo metastasis assays. Although the initial growth rates of primary tumors seeded from CRISPR-TC10-depleted MTLn3 cells were similar to primary tumors seeded from non-targeting control cells, we speculate that TC10 depletion resulted in strong defects during vascular-crossing or on secondary metastatic outgrowths. Interestingly, the circulating tumor cell counts were not significantly different between CRISPR-TC10 cells and non-targeting control cells (Supplementary Fig. 18). This result indicates that the point of impact for TC10 is more significant during the later phases of the metastatic cascade, including extravasation, the invasion at the secondary sites, or the outgrowth and metastatic colonization. The ECM degradative capacities impacted by TC10 depletion could manifest differently between initial invasion/intravasation conditions and the secondary extravasation. Moreover, the TC10 functions could be critical during the secondary outgrowth phase of metastatic cascades, as TC10 may regulate the surface expression and availability of other important cell surface receptors, including those that are associated with the cellular metabolic control such as the insulin-mediated surface transport of glucose receptors[97,98]. When CRISPR/Cas9-mediated TC10 knockout was performed in MDA-MB-231 cells, these cells entered into a senescent state and we were unable to produce stable knockouts. Similarly, MTLn3 cells showed initially an excellent ablation of TC10 expression following CRISPR/Cas9 transduction and selection, but the expression of TC10 partially recovered after continued cell culture even in the presence of a selection agent, pointing to TC10's important roles in normal cellular homeostasis. These observations further strengthen the hypothesis that metabolic alterations and growth defects at secondary sites for CRISPR-TC10-depleted cells may also have impacted the metastatic outcome. Further investigations remain necessary to better understand the changes in cellular and tissue metabolism that occur during metastatic cascades, during which TC10 may play important yet unknown roles. A full analysis of the in vivo effects of TC10 loss on metastatic capability, animal survival, or cellular metabolism is beyond the scope of this work. However, our study points to TC10 playing a critical role in facilitating an efficient metastatic spread of breast tumor cells within the metastatic cascade via targeting of MT1-MMP surface exposure at invadopodia.

Methods

Cell culture. MTLn3 cells (rat adenocarcinoma)[99] were cultured in Minimum Essential Medium (MEM, Corning, Corning, NY, USA) supplemented with 5% fetal bovine serum (FBS), 1% glutamine, and 100 I.U. penicillin and 100 µg/mL streptomycin (Invitrogen, Carlsbad, CA, USA), as previously described[100]. MDA-MB-231 (HTB-26, ATCC, Manassas, VA, USA) cells were cultured in Dulbecco's modified Eagle medium (DMEM, Corning) supplemented with 10% FBS, 1% glutamine, and penicillin/streptomycin, as previously described[58]. All cell lines were tested regularly for mycoplasma using the PCR-based assay (Stratagene, San Diego, CA, USA).

Transfection. Plasmid transfections were performed in OptiMEM, using Lipofectamine 2000 (Invitrogen). Cells were plated at 1×10^5 cells/well in a 6-well plate and incubated overnight prior to transfection. Following the manufacturer's protocols, 2 µg of total DNA was transfected into each well of a 6-well plate. Cells were treated with the transfection mixture for 45 min, and the transfection was terminated by exchanging the medium with the normal growth medium.

ECM degradation assay. Alexa Fluor 405 NHS Ester (Thermo Fisher Scientific, Waltham, MA, USA) was conjugated with 0.2% porcine gelatin (Sigma-Aldrich, St. Louis, MO, USA), according to the Thermo Fisher bioconjugation protocol. Glass coverslips (25 mm, circular #1.5, Warner Instruments, Hamden, CT, USA) were coated with 0.01% poly-L-lysine for 20 min at room temperature (RT), followed by a 15 min treatment with 0.2% glutaraldehyde in phosphate-buffered saline (PBS). The Alexa Fluor 405-labeled gelatin aliquot was centrifuged at 22,000 rcf for 10 min at RT to pellet any precipitates, the supernatant was diluted 1:20 with unlabeled 0.2% gelatin, and maintained at 37 °C. The glutaraldehyde-treated coverslips were coated with the Alexa 405-gelatin mixture for 10 min at RT, followed by a 5 min treatment with 0.2% glutaraldehyde. Then, the coverslips were incubated in 5 mg/mL $NaBH_4$ solution for 15 min at RT and washed 3× with PBS. The coverslips were placed in normal culture media at 37 °C and 5% CO_2 for at least 20 min prior to cell plating. Cells were plated at a density of 1.5×10^5 cells/coverslip in wells of a 6-well plate for 16 h before fixation with 1% paraformaldehyde (PFA) for 15 mins at RT. ECM degradation was measured by quantifying the mean area of non-fluorescent pixels per field, using a manual threshold in MetaMorph software (ver. 7.10.3; Molecular Devices, San Jose, CA, USA). For experiments in which a transgene was expressed in cells, only the degraded areas under the transfected cells, as identified by fluorescent protein expression, were considered.

EGF stimulation. EGF stimulation was performed as previously described[59,61]. In brief, MTLn3 cells were starved for 4 h in L15 media containing 0.003% bovine serum albumin (BSA) at 37 °C, without CO_2, and then stimulated with 5 nM EGF (Invitrogen) for the indicated times at 37 °C before fixation for 15 min at RT using 1% PFA.

Western blotting. Cells were lysed on ice in a buffer containing 1% NP-40, 50 mM Tris pH 7.4, 150 mM NaCl, 10 mM ethylenediaminetetraacetic acid (EDTA), 1 mM phenylmethylsulfonyl fluoride (PMSF), and 1× protease inhibitor cocktail (Sigma). The lysate was clarified by centrifugation at 22,000 rcf for 10 min at 4 °C. Lysates were resolved by 8–12% sodium dodecyl sulfate-polyacrylamide gel electrophoresis

(SDS-PAGE). Proteins were transferred to polyvinylidene fluoride membranes. After blocking for at least 1 h in 5% BSA in Tris-buffered saline containing 0.1% Tween-20 (TBS-T), membranes were incubated with primary antibodies at 1:1000 dilution overnight at 4 °C. Membranes were incubated with secondary fluorescently labeled antibodies (LI-COR Biosciences, Lincoln, NE, USA) at 1:10,000 dilution for 1 h at RT. Immunoblots were visualized using the Odyssey Imager (LI-COR Biosciences).

Antibodies. TC10 (Novus, Littleton, CO, USA; 07-2151; rabbit polyclonal used at 1:500 for western blots), p190 (BD Transduction Laboratories; 610149; Clone 30/p190; mouse monoclonal), p120 (Abcam, Cambridge, UK; ab2922; Clone B4F8; mouse monoclonal), Exo70 (Santa Cruz Biotechnology; sc-365825; Clone D-6; mouse monoclonal), Vamp7 (Abcam; ab36195; Clone 158.2; mouse monoclonal), MT1-MMP-Hinge region (Millipore, Burlington, MA, USA; AB6004; rabbit polyclonal), MT1-MMP (Millipore; MAB3328; Clone LEM-2/15.8; mouse monoclonal), MT1-MMP (Abcam; ab38971; rabbit polyclonal), Cortactin (Abcam; ab3333; Clone 0.T.21; mouse monoclonal, used at 1:600), Cortactin (Abcam; ab81208; Clone EP1922Y; rabbit monoclonal), Cortactin (Santa Cruz Biotechnology; sc-30771; G-18; goat polyclonal), MYC (Cell Signaling Technology, Danvers, MA, USA; mab2278; Clone 71D10; rabbit monoclonal), FLAG (Sigma; F1804; Clone M2; mouse monoclonal), EGFP (Roche; 11814460001; Clones 7.1 and 13.1; mixture mouse monoclonal), Rac1 (Millipore; 05-389; Clone 23A8; mouse monoclonal), Cdc42 (Santa Cruz Biotechnology; sc-8401; Clone B-8; mouse monoclonal), and RhoA (Santa Cruz Biotechnology; sc-418; Clone 26C4; mouse monoclonal). Unless otherwise stated, all primary antibodies were used at 1:200 dilution for immunofluorescence and 1:1000 for western blotting. Antibody specificities for TC10 vs Cdc42 are shown in Supplementary Figure 19z.

In vitro invasion assay. In vitro invasion assays were performed as previously described[59]. In brief, 1.5×10^5 cells were plated in the top wells of Growth Factor Reduced Matrigel-coated invasion chambers (8 µm pore size, BD Bio Coat). Media containing 5% serum was added to the lower chamber, and cells were allowed to invade along the serum gradient for 18 h at 37 °C. The assay was fixed with 3.7% PFA for 20 min and stained with NucBlue (Invitrogen) to visualize the nuclei. When siRNA-transfected cells were used, siGLO-Red (Dharmacon, Lafayette, CO, USA) was co-transfected in the cells to identify siRNA-treated cells. The membrane was detached from the chamber and mounted on a coverslip, and 10 random fields of view were imaged across the membrane at 20× magnification on an IX81-ZDC microscope (Olympus, Tokyo, Japan). The number of invading cells was counted manually with ImageJ software by thresholding onto the nucleus, and data are reported as the means of 3 experiments for each condition.

Invadopodia lifetime assay. MTLn3 cells were transfected with cortactin-miRFP703 and EGFP-Tks5[101] before plating on gelatin-coated coverslips for 16 h. The cells were imaged every 2 min for 4 h on an IX81-ZDC inverted epi-fluorescence microscope at 60× magnification (Olympus). Invadopodia lifetimes were quantified manually for at least 30 invadopodia from at least 10 cells per condition in at least 3 experiments. Control and siRNA conditions were imaged on the same day for each experiment. Cells expressing siRNA and scrRNA were identified by co-transfection with siGLO-Red (Dharmacon).

Immunoprecipitation and pull-down experiments. HEK293T cells were plated overnight at a density of 1×10^6 cells on poly-L-lysine-coated six-well plates. The FLAG-tagged TC10 mutants and the MYC-tagged WT Exo70 expression constructs were mixed at a 1:1 ratio, and the cells were transfected using the polyethyleneimine (PEI) reagent at the optimized 2 µg DNA to 8 µL PEI ratio for each well, according to published protocols[102]. After 48 h, cells were lysed in a buffer containing 1% NP-40, 20 mM Tris HCl, pH 7.4, 137 mM NaCl, 10 mM $MgCl_2$, 1 mM PMSF, and 1× protease inhibitor cocktail (Sigma-Aldrich). Lysates were clarified by centrifugation at 22,000 rcf for 10 min at 4 °C. After removing an input fraction, lysates were mixed with protein A/G agarose beads (Pierce, Waltham, MA, USA) conjugated to antibodies against FLAG-tag (Sigma-Aldrich) or Exo70 (Santa Cruz, Dallas, TX, USA), at a concentration of 2 µg antibody per sample, and incubated overnight at 4 °C with gentle rocking. Samples were washed 3× in lysis buffer, mixed with 5× gel loading buffer, and boiled for 5 min at 99 °C prior to loading and separation by SDS-PAGE for western blotting analysis.

Biosensor pull-downs were performed using purified PAK1-PBD-agarose beads, as previously described[61]. To prepare the glutathione (GSH)-agarose beads, 72 mg of GSH-agarose (Sigma-Aldrich) was resuspended in 10 ml sterile water and incubated at 4 °C for 1 h. The suspension was briefly centrifuged, and the pellet was washed three times with sterile water, followed by washing two times in a resuspension buffer (50 mM Tris, pH 8.0, 40 mM EDTA, and 25% sucrose). The washed GSH-agarose slurry was resuspended in 1 ml of resuspension buffer. To generate GST-PAK1-PBD, pGEX-PBD (a gift from G. Bokoch[103]) was transformed into BL21(DE3)-competent bacteria (Agilent Technologies, Santa Clara, CA, USA) and grown in a shaker flask at 225 rpm and 37 °C until an optical density of 1.0 at 600 nm was achieved. Protein synthesis was induced by the addition of 0.2 mM Isopropyl β-d-1-thiogalactopyranoside (IPTG), and the flask was immediately chilled to RT and incubated at 225 rpm and 24 °C overnight. The next day, bacteria were pelleted and resuspended in 20 ml resuspension buffer containing 1 mM PMSF, 1× protease inhibitor cocktail (Sigma-Aldrich), and 2 mM β–mercaptoethanol and rotated on a Nutator for 20 min at 4 °C. After incubation, 8 ml detergent buffer (50 mM Tris, pH 8.0, 100 mM $MgCl_2$, and 0.2% [wt/vol] Triton X-100) was added, and the mixture was incubated at 4 °C for 10 min on a Nutator. After incubation, the mixture was ultrasonicated (4× cycles of 30-s ultrasonication followed by 1 min rest on ice) and centrifuged at 22,000 rcf for 45 min at 4 °C. The supernatant was transferred to a 50 ml tube, and 1 ml previously prepared GSH-agarose beads were added and incubated at 4 °C for 1 h on a Nutator. The beads were then pelleted by a brief centrifugation step and washed four times with wash buffer (50 mM Tris, pH 7.6, 50 mM NaCl, and 5 mM $MgCl_2$) followed by resuspension in 500 µl of 50:50 glycerol/wash buffer. Aliquots of this mixture at 50 µl were stored at −80 °C until use. For pull-down experiments, HEK293T cells were transfected and lysed as described above. Lysates were clarified by centrifugation at 22,000 rcf for 10 min at 4 °C. After removing an input fraction, lysates were incubated with PAK1-PBD–conjugated agarose beads for 1 h at 4 °C, washed 3× in lysis buffer, resuspended in final sample buffer, and analyzed by western blotting. Incubation with Ponceau S solution (Sigma-Aldrich) was used to visualize GST-PAK1-PBD to control for equal loading. Anti-GFP (mouse; 11814460001; clones 7.1 and 13.1 mix; Roche, Basel, Switzerland) antibody was used to detect the TC10 biosensor or fluorescently tagged TC10 protein.

Generation of a TC10-knockout cell line using CRISPR-Cas9. Four different 20-nt guide sequences for TC10 were selected using the online CRISPR Design Tool (http://tools.genome-engineering.org) against rat TC10 GTPase. Sequences for the primer pairs are as follows: sgRNA 1: 5′-CACCGCGTAGTGGTCGAAGACAGT-3′ and 5′-AAACACTGTCTTCGACCACTACGC-3′; sgRNA 2: 5′-CACCGTGCG TAGTGGTCGAAGACAG-3′ and 5′-AAACCTGTCTTCGACCACTACGCAC-3′; sgRNA 3: 5′-CACCGAGGTACTGCTTGCCCCCCA-3′ and 5′-AAACTGGGGG GCAAGCAGTACCTC-3′; and sgRNA 4: 5′-CACCGGGGGGCAAGCAGTACC TCT-3′ and 5′-AAACAGAGGTACTGCTTGCCCCCC-3′. A negative control NT1 with the sequence 5′-GCGAGGTATTCGGCTCCGCG-3′ was also used, which was based on a negative control sequence from the GeCKOv2 Mouse Library Pool A[104]. sgRNAs were cloned into the pLentiCRISPR v2 plasmid[104,105] by digestion with *Bsm*BI (New England Biololabs, Ipswich, MA, USA). pLentiCRISPR v2 was a gift from F. Zhang (Massachusetts Institute of Technology, Cambridge, MA, USA; 52961; Addgene #52961, Watertown, MA, USA). The GP2-293 cell line (Takara Bio Inc., Shiga, Japan) was used to produce the lentivirus by co-transfection with pVSVg, gag-pol, rev, and tat vectors (Takara Bio Inc.). MTLn3 cells were infected with the lentivirus containing the four TC10-targeting sgRNAs or the NT1 control sgRNA and were cultured as described in the Cell Culture section. Transduced cells were selected for the stable incorporation of the CRISPR/Cas9 vector by puromycin treatment (2 µg/ml). CRISPR knockout efficiency was assessed by western blotting against TC10 (Fig. 6B). An efficient knockout population was achieved with sgRNA4, which was used for subsequent experiments.

Expression cDNA constructs. Cortactin–mtagRFP-T[83] and EGFP-Tks5[101] have been previously described. To generate cortactin-miRFP703 and mNeonGreen, mtagRFP-T was replaced with miRFP703[106] or mNeonGreen[107]. MT1-MMP-GFP was previously described[45]. VSVg-EGFP was a gift from Dr. Jennifer Lippincott-Schwartz (Addgene #11912). mCherry-Rab5a (Addgene #55126), mCherry-Rab7a (Addgene #55127), mCherry-TfR (Addgene #55144), and mCherry-Rab11a (Addgene #55124) were a gift from Dr. Michael Davidson. NPY-mCherry was a gift from Dr. Wolfhard Almers (Addgene #67156). pME pHluorin2-ratiometric was a gift from Dr. David Raible (Addgene #73794).

MT1-MMP-mCherry and MT1-MMP-pHLuorin-supercliptic were a gift from Dr. Phillipe Chavrier[44]. To construct the MT1-MMP-pHLuorin2-ratiometric, the following primer pairs were used in overlapping PCR reactions: 5′- GGATAATG TTACAAAGCTAGCGCCACCATGTCTCCCGCCCCAAGACCCTCCC-3′ and 5′- CCTTGCTCACCATGCCGCCCTCCTCGTCCACCTCAATGA-3′ for the N-terminal portion of MT1-MMP overlapping with pHLuorin2-ratiometric; 5′-GAGGAGGGCGGCATGGTGAGCAAGGGCGAGGAGCTGT-3′ and 5′-TCACC GCCCCGCCCTTGTACAGCTCGTCCATGCCGTGAGT-3′ for pHLuorin2-ratiometric; and 5′- CGAGCTGTACAAGGGCGGGGCGGTGAGCGCGGCTGC CGTGG-3′ and 5′-GGATATAAGAACAATGCGGCCGCCTAGACCTTGTCCAG CAGGGAACGCT-3′ to amplify the C-terminal portion of MT1-MMP also overlapping with pHLuorin2-ratiometric. The full-length MT1-MMP-pHLuorin2-ratiometric was PCR amplified using the primer pair: 5′-GGATAATGTTACAAAG CTAGCGCCACCATGTCTCCCGCCCCAAGACCCTCCC-3′ and 5′-GGATAT AAGAACAATGCGGCCGCCTAGACCTTGTCCAGCAGGGAACGCT-3′, and restriction digested using NheI/NotI sites and ligated into pEGFP-N1 (Clontech) backbone also digested with the compatible restriction endonucleases. pEGFP-C3-Exo70[108] was a kind gift from Dr. Channing Der (Addgene #53761). To construct the MYC-tagged Exo70, full-length human Exo70 was PCR amplified using the primer pair: 5′-GGATTATGATAGATAAGGATCCATGATTCCCCCACAGG AGGCATCCGCT-3′ and 5′-CGTATCATGATATGAATGACTCGAGTCAGG CAGAGGTGTCGAAAAGGCGATCGA-3′, followed by restriction digest using enzyme pair BamHI/XhoI. The digested fragment was ligated into the pTriEX-4 backbone that contained an N-terminal MYC-tag (pTriEX-HisMyc4)[64]. Full-length human p120RasGAP1 was a gift from Dr. Dominic Esposito (Addgene #70511). To

construct the competitive inhibitor of p190:p120 interaction, the sequence for amino acids 180 to 474 of the human p120RasGAP1 was PCR amplified, based on the sequence homology to Rat p120RasGAP1, as published previously[79]. The following primer pair was used: 5′-GGAATGTTAAGCAATGGATCCTGG TATCACGGAAAACTTGACAGAAC-3′ and 5′-CGAGTACAAGTAATTCA TCTCGAGCTAAATGTTTTTATAAAAGGCATCCTTTG-3′. The PCR amplified fragment was digested with *Bam*HI and *Xho*I and ligated into the pTriEX-4 backbone at *Bam*HI/*Xho*I sites. A codon-optimized mScarlet[109] fluorescent protein was synthesized (Genewiz, South Plainfield, NJ, USA) with an upstream *Nco*I site and a downstream 10 amino acid linker: GSGSGSGSGG (5′-GGCAGCGGCTCCG GGAGCGGGTCCGGAGGC-3′), followed by a *Bam*HI site, and inserted into the pTriEX-4 vector containing the 2-3-2 fragment at the *Nco*I/*Bam*HI sites. To produce the pTriEX-mtagBFP2 version of the p190:p120 competitive inhibitor construct, the mScarlet fluorescent protein was restriction digested with *Nco*I/ *Bam*HI, and mtagBFP2[110] was 2-step PCR-amplified using the following primer pairs: 5′-GCAATATAATGAATACCATGGTGTCTAAGGGCGAAGAGCTGAT-3′ and 5′-ACCCGCTCCCGGAGCCGCTGCCATTAAGCTTGTGCCCCAGTT TGCTA-3′, followed by 5′-GCAATATAATGAATACCATGGTGTCTAAGGGC GAAGAGCTGAT-3′ and 5′-GGTAATAAGTATATCGGATCCGCCTCCGGA CCCGCTCCCGGAGCCGCTGCCATT-3′, to encode the 10 amino acid linker GSGSGSGSGG (5′-GGCAGCGGCTCCGGGAGCGGGTCCGGAGGC-3′) followed by a *Bam*HI site. The 2-step PCR-amplified fragment was digested with *Nco*I and *Bam*HI and ligated into the pTriEX backbone containing the competitive inhibitor fragment. Full-length p190RhoGAP-A (mouse) was previously published[59]. P190RhoGAP-A mutants were produced through PCR-based site-directed mutagenesis using the Quikchange kit (Stratagene, San Diego, CA). For the Y1087F mutation, the primer pair: 5′-GGATGGATTTGATCCTTCTGACTTC GCAGAGCCCAT-3′ and 5′-ATGGGCTCTGCGAAGTCAGAAGGATCAAATCC ATCC-3′ was used. For the Y1105F mutation, the primer pair: 5′-CAAGGAATGA GGAAGAAAACATATTCTCAGTGCCCCAC-3′ and 5′-GTGGGGCACTGAGAA TATGTTTTCTTCCTCATTCCTTG-3′ was used. For the R1283A (catalytically-dead/dominant-negative) mutation, the primer pair: 5′-GCACTGAAGGCATCTA CGCGGTCAGTGGAAACAAGT-3′ and 5′-ACTTGTTTCCACTGACCGCGTA GATGCCTTCAGTGC-3′ was used. To produce a fluorescent protein-tagged p190RhoGAP-A, the following PCR primers were used:5′-GCATATATTAAGC AATCAAGAATTCATGGCAAGAAAGCAAGATGTCCGAA-3′ and 5′-GGT TTAAATATAGCATATACTCGAGCTACAGCGTGTGTTCGGCTTGGAGC-3′. The PCR fragment was digested with *Eco*RI and *Xho*I and ligated into the pTriEX backbone at corresponding *Eco*RI/*Xho*I sites, which contained the appropriate fluorescent protein at the N-terminal end of the multiple cloning site. Full-length human WT TC10 GTPase cDNA was purchased from www.cDNA.org. TC10 mutants were produced through PCR-based site-directed mutagenesis using the Quikchange kit (Stratagene). For the Q75L mutation, the primer pair: 5′-GGTCATAGTCTTCCAGTCCGGCCGTGTCA-3′ and 5′-TGACACGGCCGG ACTGGAAGACTATGACC-3′ was used. For the T31N mutation, the primer pair: 5′-CATGAGTAGGCAATTCTTGCCCACCGCCCCGTC-3′ and 5′-GACGGGG CGGTGGGCAAGAATTGCCTACTCATG-3′ was used. For the T49A mutation, the primer pair: 5′-TGGTCGAAGACGGCGGGCACGTACTCC-3′ and 5′-GGA GTACGTGCCCGCCGTCTTCGACCA-3′ was used. For the Y54C mutation, the primer pair: 5′-ACGCTGACTGCGCAGTGGTCGAAGACGG-3′ and 5′-CCGT CTTCGACCACTGCGCAGTCAGCGT-3′ was used. For the G26V mutation, the primer pair: 5′-TGCCCACCGCCACGTCGCCGACC-3′ and 5′-GGTCGGCGACG TGGCGGTGGGCA-3′ was used. For the F42L mutation, the primer pair: 5′-GCT ATGCCAACGACGCCTTACCGGAGGAGT-3′ and 5′-ACTCCTCCGGTAAGG CGTCGTTGGCATAGC-3′ was used. For the P43L/E45V/Y46H mutations, the primer pair: 5′-ACGACGCCTTCCTGGAGGTGCACGTGCCCACCG-3′ and 5′-CGGTGGGCACGTGCACCTCCAGGAAGGCGTCGT-3′ was used. For the P43L/ E45V/Y46H/T49A/Y54C mutations, the primer pair: 5′-CGACGCCTTCCTGG AGGTGCACGTGCCCGCC-3′ and 5′-GGCGGGCACGTGCACCTCCAGGAA GGCGTCG-3′ was used. To generate fusion constructs containing TC10 and fluorescent proteins or a FLAG-tag, the following primer pair was used to PCR amplify the TC10 fragment: 5′-GAGATTATTAGATGATATAGAATTCATGC CCGGAGCCGGCCGCAGCAGCAT-3′ and 5′-GCTATGCATATAATATAA TCCTCGAGTCACGTAATTAAACAACAGTTTATACATC-3′. The PCR-amplified fragment was digested with *Eco*RI/*Xho*I and ligated into the pTriEX backbone, which contained the appropriate fusion tags at *Eco*RI/*Xho*I sites. Expression constructs for the cytoskeletal RhoGTPase-targeting GEFs Dbl[64,111], Dbs[64,111], Ect2[64], Tim[64], Vav2[64], TrioGEF[61], p190RhoGEF[59,76], TEM4[112], Tiam1-C1199[64,113], Intersectin2L[62,114], GEFH1-C53R[115,116] were previously described. Expression constructs for the RabGTPase-targeting GEFs Connecdenn1, Connecdenn3, and ST5 were previously described[117]. Tiam1-DHPH-CAAX was constructed by PCR amplifying the DHPH domain fragment of mouse Tiam1 using the primer pair: 5′-gagttatatagcattagtGAATTCAAGCTGCGCAAGGTGA TCTGTGAAC-3′ and 5′-ggatattattgctagcaagaattcTTTATCTCGCAGGATCG AATGCACAG-3′, and ligated into *EcoRI* site of pTriEX-HisMyc4. CAAX box from K-Ras (KKKKKKSKTKCVIM)[118] was inserted into the C-termunus of this construct at EcoRI/XhoI by annealing and ligating into pTriEX-HisMyc4 at *EcoRI*/ *XhoI* sites, the primer pair:5′- AATTCAAGAAGAAGAAGAAGAAAAGCAAGA CCAAGTGCGTGATTATGTAGC-3′ and 5′- TCGAGCTACATAATCAC GCACTTGGTCTTGCTTTTCTTCTTCTTCTTCTTG-3′. XPLN1[119] expression constructs were constructed by PCR amplifying the DHPH fragments using the primer pairs: 5′-GCTAAATTTGTCGGAAAGAATTCTCCAAGGAAATCAAAC GTCAGGAGGCG-3′ and 5′-GCTAGCCTAAGCAATATTAGCGGCCGCTCATT ATGTTTCTTTGGCTTGACGAATACAGTT-3′ for the XPLN-DHPH, and with the reverse primer 5′-GCATAGCCTAAGCAATAAGAATTCTGTTTCTTTGGC TTGACGAATACAG-3′ for the XPLN-DHPH-CAAX, ligated into *EcoRI/NotI* of pTriEX-HisMyc4 or *EcoRI* of pTriEX-HisMyc4-CAAX, respectively. DOCK GEFs and human C3G (RapGEF1) were obtained from Dharmacon (MGC sequence-verified ORF clones; Horizons Discovery-Dharmacon). Human RapGEF2, RasGRP1, RasGRP2, and RasGRF1 were a kind gift from Dr. Dominic Esposito (Addgene #70509, 70527, 70529, and 70523, respectively). Human Sos1[120] was a kind gift from Dr. Dafna Bar-Sagi (Addgene #32920). The DOCK, RapGEFs and Sos1 were PCR amplified using the following primer pairs and inserted into pmCherry-N1 backbone at the designated restriction site pairs: mouse DOCK1-catalytic domain with *NheI/AgeI* 5′-GCATTATATCAATGAGCTAGCGCCACCA TGTACAAAGAAATTGAAAGAGAAGAGAT-3′ and 5′-CCTTAATAGATATT AAAACCGGTCCCATGGTCCTGACGCCATATTGCTTTTCCA-3′; human DOCK2-full length with *NheI/AgeI* 5′-GCATTATATCAATGAGCTAGCGCCA CCATGGCCCCCTGGCGCAAAGCTGACAA-3′ and 5′-CCTTAATAGATATT AAAACCGGTCCCAGGTCCGTGGACAGCGAGTCTGGGA-3′; human DOCK2-catalytic domain with *NheI/AgeI* 5′-GCATTATATCAATGAGCTAG CGCCACCATGTACAAAGATAACAACAGGGAGGAGAT-3′ and 5′-CCTTA ATAGATATTAAAACCGGTCCCATCTCTCGGACACCGTACTCCTTCT-3′; human DOCK4-full length with *NheI/XmaI* 5′-GCATTATATCAATGAGCTA GCGCCACCATGTGGATACCTACGGAGCACGAGAA-3′ and 5′-CCTTAATA GATATTAAACCCGGGCTAACTGAGAGACCTTGCGGGGCAGGG-3′; human DOCK4-catalytic domain with *NheI/XmaI* 5′-GCATTATATCAATGAGCTAGC GCCACCATGAAGACTGAACTGAACAAGGAGGAGAT-3′ and 5′-CCTTAAT AGATATTAAACCCGGGCCATACAAGCAGAGAACTCCTGTATCCCT-3′; human C3G (RapGEF1)-full length with *NheI/BamHI* 5′-GCATTATATCAATGA GCTAGCGCCACCATGGGCAATGCTATTGAAAAACAGAA-3′ and 5′-CCTA ATAGATATTAAGGATCCCCGGTCTTCTCTTCCCGGTCTGTTTTT-3′; and human C3G-catalytic domain with *NheI/BamHI* 5′-GCATTATATCAATG AGCTAGCGCCACCATGCACAGCCATGAGATAGCGGAGCAGCT-3′ and 5′-CCTAATAGATATTAAGGATCCCTGGGTTTAATTTTCAGAGACAGTT-3′; RapGEF2-full length with *NheI/SacII* 5′- CGTGAACCGTCAGATCCGCTA GCCACCATGGGCCAGCAGGAGAAACACTCACTTC-3′ and 5′-CGATA CAGATGGATCACATGACCGCGGTGAAACAGCAGAAACTTGTTCAT-CATCC-3′; RapGEF2-catalytic domain with *NheI/SacII* 5′-CGTGAACAGTCA GATCCGCTAGCCACCATGCTCCTTCAGCTCAGCACTGTGGAAG-3′ and 5′-CGATACTGATGTATCACAGTACCGCGGTGCTGGCTCACACTGCAGAGA-TAATGTC-3′; RapGEF3-full length with *NheI/HindIII* 5′-CGTGAACAGTC AGATACGCTAGCCACCATGAAGGTGGGCTGGCCAGGTGAGAGCT-3′ and 5′-GCATGTCTACTACAGAATACGAAGCTTTGATGGCTCCAGCTCTCG GGAGAGGCGG-3′; RapGEF3-catalytic domain with *NheI/HindIII* 5′-CGTGAACCGTCAGATCCGCTAGCCACCATGGACAACTGTCATTTCCTGC GTGTGG-3′ and 5′-GCTAGTCTACTGCATAATTCGAAGCTTCCTCG CCACCTGGCTGTCCTCGTGGAGG-3′; RapGEF4-full length with *NheI/HindIII* 5′-CGTGAACCGTCAGATCCGCTAGCCACCATGCTCTACAAGAAAT ATCGACAGTATA-3′ and 5′-GCACGTCGACTGTAGAATTCGAAGCTTCG ATGGTCGACGAGGCTCTAATCTGTGT-3′; RapGEF4-catalytic domain with *NheI/HindIII* 5′-CGTGAACCGTCAGATCCGCTAGCCACCATGCCAGA GTTGGAGAAGATTGTCAAGC-3′ and 5′-GCCCGTCGACTGCAGAATTC GAAGCTTCGATGGTCGACGAGGCTCTAATCTGTGT-3′; RasGRP1-full length with *NheI/HindIII* 5′-CGTGAACAGTCAGATATGCTAGCCACCATGGGCA CCCTGGGCAAGGCGAGAGAGG-3′ and 5′-GCCCGTCGACTGCAGAATT CGAAGCTTAGAACAGTCACCCTGCTCCATTTGAGCT-3’; RasGRP1-catalytic domain with *NheI/HindIII* 5′-CGTGAACCGTCAGATCCGCTAGCCACCA TGGTGTCTCTGGGACATTTAGCCAAAG-3′ and 5′-GCACCGTCGACTGCA GAATTCGAAGCTTGCTAATGGTTTTTGGATCAGGTTTGGG-3′; RasGRP2-full length with *NheI/XhoI* 5′-CGATAACAGTCATATTAGCTAGCCACCATG GCAGGCACCCTGGACCTGGACAAGG-3′ and 5′-CGGCAGAATTCGAAG CTTGAGCTCGAGTGACAAGTGGATGTCAAACACCCCATCC-3′; RasGRP2-catalytic domain with *NheI/XhoI* 5′-CGTGAATAGTCATATACGCTAGCCAC CATGACGGTGGAGGAGCTGCTCCGCGGGT-3′ and 5′-CGACAGAATTCG AAGCTTGAGCTCGAGCTGCAGGGACAGCTGGTACAGCTCATCC-3′; RasGRF1-full length with *NheI/SacII* 5′-CGTGAACCGTCAGATCCGCTAGCC ACCATGCAGAAGGGGATCCGGCTGAATGATG-3′ and 5′-GCTGACTA GTGGATCTCAGTACCGCGGTGAGGTGGGGAGTTTTGGTTCTATTCGG-3′; RasGRF1-catalytic domain with *NheI/SacII* 5′-CGTGAATCGTCAGATCCGC TAGCCACCATGAGACAGGAGAAGGCAGCGTGGACCA-3′ and 5′-CGATA CTGATGTATCTCTAGACCGCGGTGAGGTGGGGAGTTTTGGTTCTATTC GG-3′; and Sos1-full length with *SacI/HindIII* 5′-GCACTCAGATCTCGAGCTC GCCACCATGCAGGCGCAGCAGCTGCCCTACGAGTTTTT-3′ and 5′-CGCCG TCGACTGCAGAATTCGAAGCTTTGAGGAAGAATGGGCATTCTCCAACA GT-3′. Expression constructs for p50RhoGAP[64], Rap1GAP1[64], TBC1D10[117], and DLC-1[121] were previously described. Human TcGAP and CdGAP were obtained from Dharmacon (MGC sequence-verified ORF clones; Horizons Discovery-Dharmacon). TcGAP and CdGAP were PCR amplified using the following primer pairs and inserted into pmCherry-N1 backbone at the designated restriction site pairs: TcGAP-full length with *NheI/XmaI* 5′-GCATTATATCAATGAGCTAGC GCCACCATGGTGGCACGCAGCACTGACAGCCT-3′ and 5′-

CCATAATTAAGATAACCCGGGCGCAGTAGCTTCGGGTCTGGCCCTCAG-3′; TcGAP-catalytic domain with *NheI/XmaI* 5′-GCATTATATCAATGAGCTA GCGCCACCATGTGCGATCTTGGCGAGCACCTCAGCAA-3′ and 5′-CCATAA TTAAGATAACCCGGGCGAACAGGACGTCCACATGGGTGAGCA-3′; CdGA P-full length with *NheI/KpnI* 5′-GCATTATATCAATGAGCTAGCGCCACCA TGAAGAACAAGGGTGCTAAGCAGAA-3′ and 5′-GGTTAATATACAATTG GTACCGATTCTATTTGCCTCCCACTTCTTCCAT-3′; and CdGAP-catalytic domain with *NheI/KpnI* 5′-GCATTATATCAATGAGCTAGCGCCACCATG TGTGACCTGACGGAGTATCTGGAAAG-3′ and 5′-GGTTAATATACAATT GGTACCGAAAAGATTTGATCTACATGATTCAATA-3′.

siRNA. siRNA Smart pools for TC10, p190RhoGAP, p120RasGAP were purchased from Dharmacon/GE Healthcare (siGenome). Transfections were performed with Oligofectamine 2000 (Invitrogen) for MTLn3 cells and via electroporation, using Amaxa cell line nucleofector kit V (VACA 1003, Lonza, Basel, Switzerland), for MDA-MB-231 cells. To monitor the transfection efficiency, siGLO-Red (Dharmacon) was co-transfected, according to the manufacturer's protocols. Knockdown was assessed, and subsequent assays were performed at 48 h (MTLn3) or 72 h (MDA-MB-231) after transfection.

TC10 biosensor. A FRET biosensor for TC10 was constructed based on the previously published Rac-type, single-chain, genetically encoded biosensor backbone system[61]. Briefly, WT and mutant human TC10 GTPase sequences were PCR-amplified using the primer pair: 5′-GAGATTATTAGATGATATAGAATTCAT GCCCGGAGCCGGCCGCAGCAGCAT-3′ and 5′-GCTATGCATATAATATA ATCCTCGAGTCACGTAATTAAACAACAGTTTATACATC-3′ and restriction digested with *Eco*RI and *Xho*I. The digested fragments were ligated into the pTriEX-4 vector containing the Rac1 FRET biosensor backbone[61] at the *Eco*RI/*Xho*I sites to exchange the Rac1 GTPase sequence for the TC10 GTPase fragments. This sensor backbone was previously codon-optimized with synonymous modifications[122] to improve the stability and expression fidelity of the biosensor in target cells. To generate the retroviral vector containing the biosensor in the tet-inducible system, the pRetro-X vector system (Clontech, Mountainview, CA, USA) was used. Briefly, pRetro-X-puro (Clontech) was modified by inserting a Gateway destination (-DEST) cloning cassette (Invitrogen) into the multiple cloning site. The pTriEX-TC10 biosensor was restriction digested using *Nco*I and *Xho*I to extract the TC10 biosensor as a full-length cassette, which was then ligated into the pENTR-4 vector (Invitrogen) at *Nco*I/*Xho*I sites. The pENTR-TC10 biosensor was then processed for Gateway cloning, together with the pRetro-X-Puro-DEST vector, using LR Clonase II (Invitrogen), following the manufacturer's protocols. The resulting pRetro-X-Puro-TC10 biosensor was used to produce the retrovirus used to infect cells to produce stable/inducible tet-OFF biosensor cell lines, as previously described[68]. The sequence information for the TC10 biosensor is shown in Supplementary Data 2.

Microscopy imaging. MTLn3 or MDA-MB-231 cells were plated at a cell density of 1.5×10^5 on gelatin-coated glass coverslips. For fixed-cell imaging, cells were fixed for 15 min with 1% PFA in PBS and processed for immunofluorescence 16 h after plating. A widefield imaging modality was used to obtain immunofluorescence images. For colocalization analyses, z-stacks were imaged using 0.2-µm z-steps for 26 steps, centered on the in-focus plane, and the resultant z-stacks were deconvolved (Microvolution, Cupertino, CA, USA) to remove out of focus light. For live-cell imaging, the imaging medium was prepared by using Ham's F12K medium, without phenol red (Crystalgen, Commack, NY, USA), and supplemented with 1× GlutaMAX (Invitrogen), and sparged with Argon gas for 1 min to reduce the dissolved oxygen concentration. The medium was supplemented with 5% FBS, Oxyfluor Reagent (1:100 dilution, Oxyrase Inc., Mansfield, OH, USA), and 10 mM dl-lactate (Sigma-Aldrich)[123]. Cells were imaged at 37 °C in a closed chamber[68] mounted on an inverted microscope stage. Image acquisitions are performed through a 60× magnification objective lens (UIS 60× 1.45 NA; Olympus) using a custom microscope[124] capable of the simultaneous acquisition of FRET and mCerulean emissions through two Coolsnap ES2 cameras (Photometrics, Tucson, AZ, USA) that are mounted via an optical beam splitter and containing a T505LPXR mirror, ET480/40 M for mCerulean emission, and ET535/30 M for mVenus-FRET emission (Chroma Technology Corp, Bellows Falls, VT, USA). The relative intensities between the two channels were balanced by the inclusion of a neutral density filter (ND0.2 in mCerulean channel) to ensure that the range of brightness in both mCerulean and FRET channels were similar to maximize the signal to noise ratio. Cells were illuminated with a 100 W Hg arc lamp through a neutral density filter to attenuate light as needed and then through an ET436/20X (Chroma) bandpass filter for mCerulean excitation. The main fluorescence turret of the microscope contained a 20/80 mirror (Chroma Technology) that allowed 20% of the excitation illumination to reach the specimen and 80% of the emitted light to pass through to detection. The IX81ZDC microscope was fitted with a T555LPXR longpass mirror (Chroma) within the internal port-switching prism holder to direct the biosensor emission channels to the left-hand side port of the microscope and direct the longer wavelengths, including the cortactin and differential interference contrast (DIC) channels, to the bottom port of the microscope. The bottom port of the microscope was fitted with a single Coolsnap HQ2 camera (Photometrics) via either FF585/29 (Semrock) emission filter for mtagRFP-T to detect cortactin fluorescence or an aligned linear polarizer to detect the DIC illumination. For MT1-MMP-pHLuorin2 ratiometric imaging, cells were excited with FF390/40 (Semrock) and FF470/28 (Semrock) excitation filters successively and the fluorescence emission through ET525/50 M (Chroma) was measured and processed for ratiometric analysis. MetaMorph software (Molecular Devices) was used to control the microscope, motion control devices, and image acquisition. Metamorph and MatLab software (ver 2011a; Mathworks, Natick, MA, USA) were used to perform image processing and data analyses, as previously described[58,61,68]. Ratiometric image processing included camera noise subtraction, flatfield correction, background subtraction, image registration, ratio calculations, and correction for photobleaching[125]. In brief, camera noise images were acquired at the same exposure times as the foreground image sets but without field illumination. This represented the camera read noise and the dark current noise and was subtracted from all subsequent foreground images. Flatfield correction involved the acquisition of cell-free fields of view with the same exposure and field illumination conditions as the foreground image sets, followed by camera noise subtraction to obtain the shading images. The camera noise–subtracted foreground images were then divided by the shading images to obtain flatfield-corrected images. A small region of interest in the background (cell-free) area was selected in the flatfield-corrected foreground image sets, and the mean gray value from such a region was subtracted from the whole field of view, calculated, and processed at each time point to obtain the background-subtracted image sets. The background-subtracted image sets were then subjected to an affine transformation based on a priori calibration, to account for misalignments between the three cameras used for the simultaneous imaging of the FRET and mCerulean channels, plus the cortactin and DIC channels in the longer wavelengths. After the transformation, a linear X–Y registration was performed on the resulting image sets before ratio calculations, in which the FRET image set was divided by the mCerulean channel image set. For the MT1-MMP-pHLuorin2 ratiometric analysis, the fluorescence emission from 390 nm excitation was divided by that from 470 nm excitation. For photobleaching corrections of the FRET ratio image set, whole-cell mean gray values were calculated at each time point and fitted to a biexponential decay model. The inverse function of the regressed model was then multiplied into the ratio image set to approximate the effect of photobleaching. For fixed-cell biosensor imaging, a single Coolsnap HQ2 camera (Photometrics) attached to the bottom port of the microscope was used, together with a 60× magnification objective lens. In this case, excitation and emission filter wheels switched appropriate filter sets, in addition to the appropriate neutral density filters, to acquire mCerulean and FRET emissions plus any other additional wavelengths, as required. For the imaging of biosensors, we adjusted the camera acquisition time duration by targeting to fill approximately 80% of the total digitization range of the charge-coupled device circuitry to maximize the dynamic range, using excitation light intensities of 0.4–1.0 mW at the specimen plane.

STORM imaging. STORM (Stochastic Optical Reconstruction Microscopy) imaging was performed with a Nikon superresolution microscope equipped with a 100× oil-immersion objective (NA 1.49) and an EMCCD Andor iXon3 DU897 camera. Imaging was performed in β-mercapto-ethanol containing imaging buffer[126]. Each acquisition run had a duration of 8:00 min of continuous acquisition (camera setting in Nikon Elements software set at 1 frame). The z-position was maintained with the Nikon Perfect Focus System. The 647 nm excitation laser was set at 100% throughout each run. STORM processing was conducted in an identical manner for all runs, using the Nikon-Elements-integrated STORM Analysis routine with automatic drift correction. Minimal Peak heights were set at 100. In the superresolution image reconstruction, molecules are represented by a Gaussian spot. For the data analysis, regions of interest around invadopodia were drawn based on an intensity threshold on the widefield images corresponding to the pre-bleach epifluorescence from the cortactin immunofluorescence. The percentage areas of the reconstructed superresolution Gaussian spots within such regions of interest around invadopodia were determined for each invadopodium. Only the invadopodia regions of interest that were equal to or greater than 10 square pixels area were processed for the analysis.

TIRF imaging. Total internal reflection fluorescence (TIRF) microscopy imaging was performed with the Orbital 200 laser ring TIRF system (Visitron Systems), installed on an Olympus IX81ZDC microscope, with a 1.45NA 60× oil-immersion objective lens. The TIRF laser angles were calibrated at each wavelength and set such that the illumination penetration depth was 360 nm from the surface of the coverslip to achieve a modest HiLo-illumination condition. Photometrics PrimeBSI sCMOS camera was used at 1 × 1 binning, and the time-lapse imaging sequence was controlled by Visiview software (version 5.0.0.8, Visitron Systems).

Colocalization analysis. Deconvolved z-stack images of cells coexpressing TC10 and other vesicular markers were selected for the best in-focus plane, and analyzed for colocalization using ImageJ plugin *Coloc2*, by setting a region of interest around the cell being analyzed and maintaining the parameters as default Costes threshold regression and the point spread function of 3-pixels, and the randomization parameter was set to 10.

Fluorometric characterization and validation of the biosensor. The characterization of the biosensor response was performed in HEK293T cells by transiently overexpressing WT or mutant versions of the biosensor with or without the appropriate upstream regulators, as described previously[63,127]. In brief, HEK293T cells were plated overnight at 1×10^6 cells/well in six-well plates coated with poly-L-lysine (Sigma-Aldrich) and transfected the following day using PEI reagent according to the published optimized procedures[102]. For suspended cell measurements, after 48 h transfection, cells were serum-starved for 6 h in culture medium containing 2.0% BSA without serum, washed once with PBS, briefly trypsinized, and resuspended in 500 µL of cold PBS per well. Cell suspensions were stored on ice until assay. Fluorescence emission spectra were measured with a spectrofluorometer (Horiba-Jobin-Yvon Fluorolog-3MF2; HORIBA, Kyoto, Japan). The fluorescence emission spectra were obtained by exciting the cell suspension in a 500 µL quartz cuvette (Starna Cells, Atascadero, CA, USA) at 433 nm, and emission fluorescence was scanned between 450–600 nm. For adhered cell measurements, after 48 h transfection, cells were fixed in 1.0 % formaldehyde in PBS for 15 min, washed twice with PBS, and processed immediately for fluorometric spectral scanning in a plate-reader attachment to the spectrofluorometer (MicroMax384; HORIBA). The background fluorescence reading of cells containing an empty vector (pCDNA3.1) was used to measure light scatter and autofluorescence and was subtracted from the data. The resulting spectra were normalized to the peak of the donor mCerulean emission intensity at 474 nm to generate the final ratiometric spectra. To validate the biosensor in cancer cells using exogenous stimulation, MTLn3 cells transiently expressing the biosensor were serum-starved for 4 h and stimulated using medium containing 5% serum or 5 nM EGF. Cells were fixed and imaged at 0, 1, 2, and 3 min after stimulation and analyzed for changes in the FRET/donor ratio.

Biosensor activity analysis at invadopodia. A time-lapse series of the region of interest containing an invadopodium was analyzed first by producing time projections. The cortactin core location image was calculated by obtaining the median projection, over time, of the cortactin channel. TC10 activity localizations were calculated by taking the summation of intensities overtime at the invadopodium region of interest in a time-lapse stack, as previously described for a different class of Rho GTPase activity measurements at invadopodia[59]. Line scans were measured and averaged over 4 perpendicular lines that were centered on the core of the cortactin spot, with each line rotationally 45 degrees apart. Line scans were normalized to the local maxima of TC10 activity at the ring-like region surrounding the invadopodia core, which was denoted by the cortactin spot. The cortactin intensity was normalized at the center position, taken as the maximal intensity location along with the line scans.

For experiments measuring the frequency ratio of high biosensor activity at invadopodia during transient invadopodia formation, we identified regions of cells featuring the formation of nascent invadopodium in a time-lapse experiment under steady-state conditions. The cortactin image stack was used to identify and select an elliptical region of interest in which the invadopodium core was transiently developing. A random region was also chosen away from all cortactin spots to serve as the background, and both regions were tracked for average intensity values over the entire time course of an experiment. The regions of interest were transferred to the respective biosensor ratio data stack, and the average biosensor intensity values were also measured as a function of time. The average foreground intensities over time and the standard deviation (SD) were calculated from the data, as follows: for data corresponding to the regions with cortactin spot formation, the average and SD were calculated up to the time point at which a nascent invadopodia formation became visible; for the random background control region, the average and SD were measured for the entire duration of the time-lapse experiment. The data were then thresholded at +1.0 SD away from the mean, and any activity values above this threshold were considered to be positive biosensor activity events. The total number of positive biosensor activity events were divided by the total number of time points in the corresponding time domains (before or during invadopodia formation, as determined from the cortactin data stack), and the resulting positive activity event per time data during invadopodia formation were normalized against the values from before invadopodia formation.

Autocorrelation analysis for periodicity. For the fluctuation analysis, a binary mask was created in MetaMorph using cortactin fluorescence intensity as a reference to designate the core of the invadopodium. Subsequently, this mask was dilated 30 pixels, and the original core was subtracted to generate a binary mask to designate the invadopodia ring-like region surrounding the core. These binary masks were used to measure the intensity in each compartment of the invadopodium. The area of the ring was based on a spatial distance of 1.74 µm radius outside of the core, which is similar to the binary mask used in a previous work[59]. To quantitatively determine the periodicity of biosensor activity fluctuations within the core of an invadopodium versus the ring surrounding the invadopodium, a time series of the ratio of intensities was measured within binary masks that were generated to target either the invadopodium core or the ring surrounding the invadopodium core. These ratio time series were analyzed using the autocorrelation function *xcov* in MatLab. The individual autocorrelation function distribution was smooth-spline fitted, pooled between all invadopodia analyzed in all cells, and the mean autocorrelation function and 95% confidence intervals were calculated by a nonparametric bootstrap method[128]. The measured temporal width to the peaks of the first side lobes after the zero-crossing was taken as the period of oscillation[69,36]. Our data sampling rate was the frequency of image acquisition at 10 s intervals, which enabled us to characterize small fluctuations with a characteristic periodicity of up to approximately 2× this sampling rate based on the Nyquist-Shannon sampling theorem[129]. As such, we applied a smoothing filter to the data by taking a running average of three sampling time steps at a time. This filter operation therefore conservatively approximates a slightly longer sampling frequency of 30 s intervals, enabling us to characterize fluctuations that are in the order of 1 min or longer periodic behaviors. Our total data acquisition time-lapse duration was typically 60–90 frames (10–15 min). This enabled at a maximum greater than 2× oversampling of the complete periodic cycles within this time duration since our sampling frequency and the post-process filtrations timings were sufficiently short.

Proximity ligation assay. The TC10 and Exo70 interaction was detected in situ using Duolink In Situ Red Kit Mouse/Rabbit (Sigma) according to the manufacturer's protocols. Briefly, MTLn3 cells were transfected with Flag-tagged TC10 wild-type or 5 × mutant, together with MYC-tagged Exo70 wild-type and mNeonGreen-cortactin, using Lipofectamine 2000 as described. Cells were fixed in 3.7% formaldehyde for 15 min at room temperature and permeabilized using 0.3% Triton X-100 in DPBS for 15 min. The fixed and permeabilized cells were blocked using the kit-supplied blocking reagent in a pre-heated humidity chamber for 30 min at 37 °C. Anti-MYC rabbit monoclonal antibody clone 71D10 (Cell Signaling Technology) and anti-Flag mouse monoclonal antibody clone M2 (Sigma) were diluted 1:200 in the kit-supplied antibody dilution buffer. The cells were incubated with the primary antibodies for 1 h at 37 °C in a pre-heated humidity chamber. PLA probes (mouse-MINUS and rabbit-PLUS) mixture were used at a 1:5 dilution of each probe and incubated for 1 h at 37 °C in a pre-heated humidity chamber, followed by ligation and amplification reactions according to the manufacturer's protocol. Nuclei were stained with NucBlue dye (Invitrogen). Images were acquired on an Olympus IX81ZDC epifluorescence microscope with 60 × 1.45 NA objective lens. The invadopodia were identified using mNeonGreen cortactin fluorescence, and the presence of PLA spots in the red fluorescence channel was quantified by drawing a region of interest around the invadopodia and identifying those spots that either colocalized, flanked, or not localized at invadopodia.

Analysis of tumor intravasation and metastasis in vivo. MTLn3 cells that stably expressed EGFP and featured the CRISPR/Cas9-mediated TC10 deletion were injected into the mammary glands of female SCID mice (6–8-week-old; Jackson ImmunoResearch Laboratories, Inc., West Grove, PA, USA[130]). A total of 1.0×10^6 cells were trypsinized and resuspended in 100 µl PBS for injection into each mouse (CRISPR/Cas9 non-targeting control, $n = 20$ mice; TC10-knockout, $n = 20$ mice). Mice were sacrificed 3–4 week after injection when the primary tumor reached 1 cm in diameter. Lung metastases were confirmed and counted at necropsy using a fluorescent microscope to image EGFP fluorescence in freshly excised and isolated lungs mounted on a microscope coverslip. Twenty randomly selected fields of view at 10× magnification per mouse lung (10 fields of view per lung lobe) were analyzed to determine the ratio between total EGFP fluorescence and background fluorescence. To quantify the circulating tumor cell counts, 1 ml of mouse blood, obtained through cardiopuncture at the time of euthanasia, was lysed in red blood cell lysis buffer (04-4300-54; Thermo Fisher Scientific/eBioscience, San Diego, CA, USA), according to the manufacturer's protocols. The remaining cells were plated into MTLn3 growth media and cultured for one additional week. The numbers of EGFP-positive MTLn3 cells were quantified in 1/4 of the area of a 10 cm tissue culture dish for each animal. All animal experiments were performed in accordance with a protocol approved by the Office of the Institutional Animal Care and Use Committee of the Albert Einstein College of Medicine (protocol 20170507). For data analysis, mice with primary tumors that showed indications of ulceration or intraperitoneal growths were omitted from the final tally.

Statistical analysis and reproducibility. All statistical significance based on p-values were calculated using a Student's *t*-test, unless stated otherwise in the figure legend. No statistical methods were used to pre-determine the sample size. No randomizations were used. The investigators were not blinded to allocation during experiments and outcome assessment. Statistical tests used are stated on every figure legend with p-values as appropriate. Data distribution should meet the normal distribution requirements. No estimate of variation. No pre-established criteria were used to determine data inclusion or exclusion.

Reporting summary. Further information on research design is available in the Nature Research Reporting Summary linked to this article.

Data availability

The raw data that support the findings of this study are available from the corresponding author on request. The source data for graphs in the main panel figures are provided in Supplementary Data 3.

Code availability

All Matlab codes and Metamorph scripts used were previously published elsewhere[69,70,125], but are also available from the corresponding author on request.

Received: 23 November 2020; Accepted: 23 August 2021;.
Published online: 16 September 2021

References

1. Sutoh, M. et al. Invadopodia formation by bladder tumor cells. *Oncol. Res* **19**, 85–92 (2010).
2. Genot, E. & Gligorijevic, B. Invadosomes in their natural habitat. *Eur. J. Cell Biol.* **93**, 367–379 (2014).
3. Bergman, A., Condeelis, J. S. & Gligorijevic, B. Invadopodia in context. *Cell Adh Migr.* **8**, 273–279 (2014).
4. Hulit, J. et al. The use of fluorescent proteins for intravital imaging of cancer cell invasion. *Methods Mol. Biol.* **872**, 15–30 (2012).
5. Gligorijevic, B. et al. N-WASP-mediated invadopodium formation is involved in intravasation and lung metastasis of mammary tumors. *J. Cell Sci.* **125**, 724–734 (2012).
6. Harney, A. S. et al. Real-time imaging reveals local, transient vascular permeability, and tumor cell intravasation stimulated by TIE2hi macrophage-derived VEGFA. *Cancer Discov.* **5**, 932–943 (2015).
7. Pignatelli, J. et al. Macrophage-dependent tumor cell transendothelial migration is mediated by Notch1/MenaINV-initiated invadopodium formation. *Sci. Rep.* **6**, 37874 (2016).
8. Stoletov, K. & Lewis, J. D. Invadopodia: a new therapeutic target to block cancer metastasis. *Expert Rev. Anticancer Ther.* **15**, 733–735 (2015).
9. Tokui, N. et al. Extravasation during bladder cancer metastasis requires cortactinmediated invadopodia formation. *Mol. Med Rep.* **9**, 1142–1146 (2014).
10. Leong, H. S. et al. Invadopodia are required for cancer cell extravasation and are a therapeutic target for metastasis. *Cell reports* **8**, 1558–1570 (2014).
11. Paz, H., Pathak, N. & Yang, J. Invading one step at a time: the role of invadopodia in tumor metastasis. Oncogene 33, 4193–4202 (2014).
12. Itoh, Y. MT1-MMP: a key regulator of cell migration in tissue. *IUBMB Life* **58**, 589–596 (2006).
13. Yamaguchi, H. Pathological roles of invadopodia in cancer invasion and metastasis. *Eur. J. Cell Biol.* **91**, 902–907 (2012).
14. Lohmer, L. L., Kelley, L. C., Hagedorn, E. J. & Sherwood, D. R. Invadopodia and basement membrane invasion in vivo. *Cell Adh Migr.* **8**, 246–255 (2014).
15. Jiang, W. G. et al. Expression of membrane type-1 matrix metalloproteinase, MT1-MMP in human breast cancer and its impact on invasiveness of breast cancer cells. *Int J. Mol. Med.* **17**, 583–590 (2006).
16. Szabova, L., Chrysovergis, K., Yamada, S. S. & Holmbeck, K. MT1-MMP is required for efficient tumor dissemination in experimental metastatic disease. *Oncogene* **27**, 3274–3281 (2008).
17. Linder, S. MT1-MMP: Endosomal delivery drives breast cancer metastasis. *J. Cell Biol.* **211**, 215–217 (2015).
18. Paterson, E. K. & Courtneidge, S. A. Invadosomes are coming: new insights into function and disease relevance. *FEBS J.* **285**, 8–27, (2018).
19. Eddy, R. J., Weidmann, M. D., Sharma, V. P. & Condeelis, J. S. Tumor Cell Invadopodia: Invasive Protrusions that Orchestrate Metastasis. *Trends Cell Biol.* https://doi.org/10.1016/j.tcb.2017.03.003 (2017).
20. Meirson, T. & Gil-Henn, H. Targeting invadopodia for blocking breast cancer metastasis. *Drug Resistance Updates: Rev. Commentaries antimicrobial anticancer Chemother.* **39**, 1–17 (2018).
21. Coussens, L. M., Fingleton, B. & Matrisian, L. M. Matrix metalloproteinase inhibitors and cancer: trials and tribulations. *Science* **295**, 2387–2392 (2002).
22. Fingleton, B. MMPs as therapeutic targets—still a viable option? *Semin Cell Dev. Biol.* **19**, 61–68 (2008).
23. Narumiya, S., Tanji, M. & Ishizaki, T. Rho signaling, ROCK and mDia1, in transformation, metastasis and invasion. *Cancer Metastasis Rev.* **28**, 65–76 (2009).
24. Yamaguchi, H. et al. Molecular mechanisms of invadopodium formation: the role of the N-WASP-Arp2/3 complex pathway and cofilin. *J. Cell Biol.* **168**, 441–452 (2005).
25. Sabeh, F., Li, X. Y., Saunders, T. L., Rowe, R. G. & Weiss, S. J. Secreted versus membrane-anchored collagenases: relative roles in fibroblast-dependent collagenolysis and invasion. *J. Biol. Chem.* **284**, 23001–23011 (2009).
26. Wisdom, K. M. et al. Matrix mechanical plasticity regulates cancer cell migration through confining microenvironments. *Nat. Commun.* **9**, 4144 (2018).
27. Vega, F. M. & Ridley, A. J. SnapShot: Rho family GTPases. *Cell* **129**, 1430 (2007).
28. Murphy, G. A. et al. Cellular functions of TC10, a Rho family GTPase: regulation of morphology, signal transduction and cell growth. *Oncogene* **18**, 3831–3845 (1999).
29. Murphy, G. A. et al. Signaling mediated by the closely related mammalian Rho family GTPases TC10 and Cdc42 suggests distinct functional pathways. *Cell Growth Differ.* **12**, 157–167 (2001).
30. Zhang, J. et al. Down-regulation of microRNA-9 leads to activation of IL-6/Jak/STAT3 pathway through directly targeting IL-6 in HeLa cell. *Mol. Carcinog.* **55**, 732–742 (2016).
31. Han, S. W. et al. RNA editing in RHOQ promotes invasion potential in colorectal cancer. *J. Exp. Med.* **211**, 613–621 (2014).
32. Chiang, S. H. et al. Insulin-stimulated GLUT4 translocation requires the CAP-dependent activation of TC10. *Nature* **410**, 944–948 (2001).
33. Goicoechea, S. M., Awadia, S. & Garcia-Mata, R. I'm coming to GEF you: Regulation of RhoGEFs during cell migration. *Cell Adh Migr* **8**, 535–549 (2014).
34. Cherfils, J. & Zeghouf, M. Regulation of small GTPases by GEFs, GAPs, and GDIs. *Physiol. Rev.* **93**, 269–309 (2013).
35. Kawase, K. et al. GTP hydrolysis by the Rho family GTPase TC10 promotes exocytic vesicle fusion. *Dev. Cell* **11**, 411–421 (2006).
36. Hsu, S. C., TerBush, D., Abraham, M. & Guo, W. The exocyst complex in polarized exocytosis. *Int Rev. Cytol.* **233**, 243–265 (2004).
37. Munson, M. & Novick, P. The exocyst defrocked, a framework of rods revealed. *Nat. Struct. Mol. Biol.* **13**, 577–581 (2006).
38. Dupraz, S. et al. The TC10-Exo70 complex is essential for membrane expansion and axonal specification in developing neurons. *J. Neurosci.* **29**, 13292–13301 (2009).
39. Monteiro, P. et al. Endosomal WASH and exocyst complexes control exocytosis of MT1-MMP at invadopodia. *J. Cell Biol.* **203**, 1063–1079 (2013).
40. Kanzaki, M. & Pessin, J. E. Caveolin-associated filamentous actin (Cav-actin) defines a novel F-actin structure in adipocytes. *J. Biol. Chem.* **277**, 25867–25869 (2002).
41. Bogan, J. S. Regulation of glucose transporter translocation in health and diabetes. *Annu Rev. Biochem* **81**, 507–532 (2012).
42. Beaty, B. T. et al. beta1 integrin regulates Arg to promote invadopodial maturation and matrix degradation. *Mol. Biol. Cell* **24**, S1661–1611 (2013).
43. Bravo-Cordero, J. J., Magalhaes, M. A., Eddy, R. J., Hodgson, L. & Condeelis, J. Functions of cofilin in cell locomotion and invasion. *Nat. Rev. Mol. Cell Biol.* **14**, 405–417 (2013).
44. Steffen, A. et al. MT1-MMP-dependent invasion is regulated by TI-VAMP/VAMP7. *Curr. Biol.* **18**, 926–931 (2008).
45. Bravo-Cordero, J. J. et al. MT1-MMP proinvasive activity is regulated by a novel Rab8-dependent exocytic pathway. *Embo J.* **26**, 1499–1510 (2007).
46. Wiesner, C., El Azzouzi, K. & Linder, S. A specific subset of RabGTPases controls cell surface exposure of MT1-MMP, extracellular matrix degradation and three-dimensional invasion of macrophages. *J. Cell Sci.* **126**, 2820–2833 (2013).
47. Gonzalez-Jamett, A. M. et al. The F-actin binding protein cortactin regulates the dynamics of the exocytotic fusion pore through its SH3 domain. *Front Cell Neurosci.* **11**, 130 (2017).
48. Clark, E. S. & Weaver, A. M. A new role for cortactin in invadopodia: regulation of protease secretion. *Eur. J. Cell Biol.* **87**, 581–590 (2008).
49. Remacle, A., Murphy, G. & Roghi, C. Membrane type I-matrix metalloproteinase (MT1-MMP) is internalised by two different pathways and is recycled to the cell surface. *J. Cell Sci.* **116**, 3905–3916 (2003).
50. Sakurai-Yageta, M. et al. The interaction of IQGAP1 with the exocyst complex is required for tumor cell invasion downstream of Cdc42 and RhoA. *J. Cell Biol.* **181**, 985–998 (2008).
51. Mahon, M. J. pHluorin2: an enhanced, ratiometric, pH-sensitive green florescent protein. *Adv. Biosci. Biotechnol.* **2**, 132–137 (2011).
52. Hoshino, D. et al. Exosome secretion is enhanced by invadopodia and drives invasive behavior. *Cell Rep.* **5**, 1159–1168 (2013).
53. Liu, J., Yue, P., Artym, V. V., Mueller, S. C. & Guo, W. The role of the exocyst in matrix metalloproteinase secretion and actin dynamics during tumor cell invadopodia formation. *Mol. Biol. Cell* **20**, 3763–3771 (2009).
54. Inoue, M., Chang, L., Hwang, J., Chiang, S. H. & Saltiel, A. R. The exocyst complex is required for targeting of Glut4 to the plasma membrane by insulin. *Nature* **422**, 629–633 (2003).
55. Wu, M., Wu, Z. F., Rosenthal, D. T., Rhee, E. M. & Merajver, S. D. Characterization of the roles of RHOC and RHOA GTPases in invasion, motility, and matrix adhesion in inflammatory and aggressive breast cancers. *Cancer* **116**, 2768–2782 (2010).
56. Ory, S. & Gasman, S. Rho GTPases and exocytosis: what are the molecular links? *Semin Cell Dev. Biol.* **22**, 27–32 (2011).
57. Johnson, D. I. Cdc42: An essential Rho-type GTPase controlling eukaryotic cell polarity. *Microbiol Mol. Biol. Rev.* **63**, 54–105 (1999).

58. Donnelly, S. K. et al. Rac3 regulates breast cancer invasion and metastasis by controlling adhesion and matrix degradation. *J. Cell Biol.* **216**, 4331–4349 (2017).
59. Bravo-Cordero, J. J. et al. A novel spatiotemporal rhoc activation pathway locally regulates cofilin activity at invadopodia. *Curr Biol* **21**, 635-644 (2011).
60. Miskolci, V., Wu, B., Moshfegh, Y., Cox, D. & Hodgson, L. Optical tools to study the isoform-specific roles of small GTPases in immune cells. *J. Immunol.* **196**, 3479–3493 (2016).
61. Moshfegh, Y., Bravo-Cordero, J. J., Miskolci, V., Condeelis, J. & Hodgson, L. A Trio-Rac1-Pak1 signalling axis drives invadopodia disassembly. *Nat. Cell Biol.* **16**, 574–586 (2014).
62. Hanna, S., Miskolci, V., Cox, D. & Hodgson, L. A new genetically encoded single-chain biosensor for Cdc42 based on FRET, useful for live-cell imaging. *PLoS One* **9**, e96469 (2014).
63. Hodgson, L., Pertz, O. & Hahn, K. M. Design and optimization of genetically encoded fluorescent biosensors: GTPase biosensors. *Methods Cell Biol.* **85**, 63–81 (2008).
64. Pertz, O., Hodgson, L., Klemke, R. L. & Hahn, K. M. Spatiotemporal dynamics of RhoA activity in migrating cells. *Nature* **440**, 1069–1072 (2006).
65. Wu, B., Chen, J. & Singer, R. H. Background free imaging of single mRNAs in live cells using split fluorescent proteins. *Sci. Rep.* **4**, 3615 (2014).
66. Ogawa, H., Inouye, S., Tsuji, F. I., Yasuda, K. & Umesono, K. Localization, trafficking, and temperature-dependence of the Aequorea green fluorescent protein in cultured vertebrate cells. *Proc. Natl Acad. Sci. USA* **92**, 11899–11903 (1995).
67. Shcherbakova, D. M., Cox Cammer, N., Huisman, T. M., Verkhusha, V. V. & Hodgson, L. Direct multiplex imaging and optogenetics of Rho GTPases enabled by near-infrared FRET. *Nat. Chem. Biol.* **14**, 591–600 (2018).
68. Bravo-Cordero, J. J., Moshfegh, Y., Condeelis, J. & Hodgson, L. Live Cell Imaging of RhoGTPase Biosensors in Tumor Cells. *Methods Mol. Biol.* **1046**, 359–370 (2013).
69. Machacek, M. et al. Coordination of Rho GTPase activities during cell protrusion. *Nature* **461**, 99–103 (2009).
70. Hodgson, L. et al. FRET binding antenna reports spatiotemporal dynamics of GDI-Cdc42 GTPase interactions. *Nat. Chem. Biol.* **12**, 802–809 (2016).
71. Arthur, W. T. & Burridge, K. RhoA inactivation by p190RhoGAP regulates cell spreading and migration by promoting membrane protrusion and polarity. *Mol. Biol. Cell* **12**, 2711–2720 (2001).
72. Bidaud-Meynard, A., Biname, F., Lagree, V. & Moreau, V. Regulation of Rho GTPase activity at the leading edge of migrating cells by p190RhoGAP. *Small GTPases*, 1–12, https://doi.org/10.1080/21541248.2017.1280584 (2017).
73. Fujita, A. et al. GTP hydrolysis of TC10 promotes neurite outgrowth through exocytic fusion of Rab11- and L1-containing vesicles by releasing exocyst component Exo70. *PLoS One* **8**, e79689 (2013).
74. Nakahara, H. et al. Activation of beta1 integrin signaling stimulates tyrosine phosphorylation of p190RhoGAP and membrane-protrusive activities at invadopodia. *J. Biol. Chem.* **273**, 9–12 (1998).
75. Magalhaes, M. A. et al. Cortactin phosphorylation regulates cell invasion through a pH-dependent pathway. *J. Cell Biol.* **195**, 903–920 (2011).
76. Bravo-Cordero, J. J. et al. Spatial regulation of RhoC activity defines protrusion formation in migrating cells. *J. Cell Sci.* **126**, 3356–3369 (2013).
77. Wu, Y. I. et al. A genetically encoded photoactivatable Rac controls the motility of living cells. *Nature* **461**, 104–108 (2018).
78. Bradley, W. D., Hernandez, S. E., Settleman, J. & Koleske, A. J. Integrin signaling through Arg activates p190RhoGAP by promoting its binding to p120RasGAP and recruitment to the membrane. *Mol. Biol. Cell* **17**, 4827–4836 (2006).
79. Tomar, A., Lim, S. T., Lim, Y. & Schlaepfer, D. D. A FAK-p120RasGAP-p190RhoGAP complex regulates polarity in migrating cells. *J. Cell Sci.* **122**, 1852–1862 (2009).
80. Mader, C. C. et al. An EGFR-Src-Arg-cortactin pathway mediates functional maturation of invadopodia and breast cancer cell invasion. *Cancer Res* **71**, 1730–1741 (2011).
81. Razidlo, G. L., Schroeder, B., Chen, J., Billadeau, D. D. & McNiven, M. A. Vav1 as a central regulator of invadopodia assembly. *Curr. Biol.* **24**, 86–93 (2014).
82. Liu, B. P. & Burridge, K. Vav2 activates Rac1, Cdc42, and RhoA downstream from growth factor receptors but not beta1 integrins. *Mol. Cell Biol.* **20**, 7160–7169 (2000).
83. Oser, M. et al. Cortactin regulates cofilin and N-WASp activities to control the stages of invadopodium assembly and maturation. *J. Cell Biol.* **186**, 571–587 (2009).
84. Yamaguchi, H. & Condeelis, J. Regulation of the actin cytoskeleton in cancer cell migration and invasion. *Biochim Biophys. Acta* **1773**, 642–652 (2007).
85. Albiges-Rizo, C., Destaing, O., Fourcade, B., Planus, E. & Block, M. R. Actin machinery and mechanosensitivity in invadopodia, podosomes and focal adhesions. *J. Cell Sci.* **122**, 3037–3049 (2009).
86. Parekh, A. et al. Sensing and modulation of invadopodia across a wide range of rigidities. *Biophys. J.* **100**, 573–582 (2011).
87. Chang, J., Pang, E. M., Adebowale, K., Wisdom, K. M. & Chaudhuri, O. Increased stiffness inhibits invadopodia formation and cell migration in 3D. *Biophys. J.* **119**, 726–736 (2020).
88. Dalaka, E. et al. Direct measurement of vertical forces shows correlation between mechanical activity and proteolytic ability of invadopodia. *Sci. Adv.* **6**, eaax6912 (2020).
89. Cambi, A. & Chavrier, P. Tissue remodeling by invadosomes. *Fac. Rev.* **10**, 39 (2021).
90. Settleman, J., Albright, C. F., Foster, L. C. & Weinberg, R. A. Association between GTPase activators for Rho and Ras families. *Nature* **359**, 153–154 (1992).
91. Muller, P. M. et al. Systems analysis of RhoGEF and RhoGAP regulatory proteins reveals spatially organized RAC1 signalling from integrin adhesions. *Nat. Cell Biol.* **22**, 498–511 (2020).
92. Marchesin, V. et al. ARF6-JIP3/4 regulate endosomal tubules for MT1-MMP exocytosis in cancer invasion. *J. Cell Biol.* **211**, 339–358 (2015).
93. Hu, K. Q. & Settleman, J. Tandem SH2 binding sites mediate the RasGAP-RhoGAP interaction: a conformational mechanism for SH3 domain regulation. *EMBO J.* **16**, 473–483 (1997).
94. Warren, M. S. et al. Integrin beta1 signals through Arg to regulate postnatal dendritic arborization, synapse density, and behavior. *J. Neurosci.* **32**, 2824–2834 (2012).
95. Simpson, M. A. et al. Direct interactions with the integrin beta1 cytoplasmic tail activate the Abl2/Arg kinase. *J. Biol. Chem.* **290**, 8360–8372 (2015).
96. Mai, A. et al. Competitive binding of Rab21 and p120RasGAP to integrins regulates receptor traffic and migration. *J. Cell Biol.* **194**, 291–306 (2011).
97. Chiang, S. H., Chang, L. & Saltiel, A. R. TC10 and insulin-stimulated glucose transport. *Methods Enzymol.* **406**, 701–714 (2006).
98. Bridges, D., Chang, L., Lodhi, I. J., Clark, N. A. & Saltiel, A. R. TC10 is regulated by caveolin in 3T3-L1 adipocytes. *PLoS One* **7**, e42451 (2012).
99. Neri, A. & Nicolson, G. L. Phenotypic drift of metastatic and cell-surface properties of mammary adenocarcinoma cell clones during growth in vitro. *Int J. Cancer* **28**, 731–738 (1981).
100. Segall, J. E. et al. EGF stimulates lamellipod extension in metastatic mammary adenocarcinoma cells by an actin-dependent mechanism. *Clin. Exp. Metast* **14**, 61–72 (1996).
101. Courtneidge, S. A., Azucena, E. F., Pass, I., Seals, D. F. & Tesfay, L. The SRC substrate Tks5, podosomes (invadopodia), and cancer cell invasion. *Cold Spring Harb. Symp. Quant. Biol.* **70**, 167–171 (2005).
102. Ehrhardt, C. et al. Polyethylenimine, a cost-effective transfection reagent. *Signal Transduct.* **6**, 179–184 (2006).
103. Benard, V. & Bokoch, G. M. Assay of Cdc42, Rac, and Rho GTPase activation by affinity methods. *Methods Enzymol.* **345**, 349–359 (2002).
104. Shalem, O. et al. Genome-scale CRISPR-Cas9 knockout screening in human cells. *Science* **343**, 84–87 (2014).
105. Sanjana, N. E., Shalem, O. & Zhang, F. Improved vectors and genome-wide libraries for CRISPR screening. *Nat. Methods* **11**, 783–784 (2014).
106. Shcherbakova, D. M. et al. Bright monomeric near-infrared fluorescent proteins as tags and biosensors for multiscale imaging. *Nat. Commun.* **7**, 12405 (2016).
107. Shaner, N. C. et al. A bright monomeric green fluorescent protein derived from Branchiostoma lanceolatum. *Nat. Methods* **10**, 407–409 (2013).
108. Martin, T. D. et al. Ral and Rheb GTPase activating proteins integrate mTOR and GTPase signaling in aging, autophagy, and tumor cell invasion. *Mol. Cell* **53**, 209–220 (2014).
109. Bindels, D. S. et al. mScarlet: a bright monomeric red fluorescent protein for cellular imaging. *Nat. Methods* **14**, 53–56 (2017).
110. Subach, O. M., Cranfill, P. J., Davidson, M. W. & Verkhusha, V. V. An enhanced monomeric blue fluorescent protein with the high chemical stability of the chromophore. *PLoS One* **6**, e28674 (2011).
111. Snyder, J. T. et al. Quantitative analysis of the effect of phosphoinositide interactions on the function of Dbl family proteins. *J. Biol. Chem.* **276**, 45868–45875 (2001).
112. Mitin, N., Rossman, K. L. & Der, C. J. Identification of a novel actin-binding domain within the Rho guanine nucleotide exchange factor TEM4. *PLoS One* **7**, e41876 (2012).
113. Michiels, F., Habets, G. G. M., Stam, J. C., vander Kammen, R. A. & Collard, J. G. A role for rac in tiam 1-induced membrane ruffling and invasion. *Nature* **375**, 338–340 (1995).
114. Klein, I. K. et al. Intersectin-2L regulates caveola endocytosis secondary to Cdc42-mediated actin polymerization. *J. Biol. Chem.* **284**, 25953–25961 (2009).
115. Krendel, M., Zenke, F. T. & Bokoch, G. M. Nucleotide exchange factor GEF-H1 mediates cross-talk between microtubules and the actin cytoskeleton. *Nat. Cell Biol.* **4**, 294–301 (2002).

116. Zenke, F. T. et al. p21-activated kinase 1 phosphorylates and regulates 14-3-3 binding to GEF-H1, a microtubule-localized Rho exchange factor. *J. Biol. Chem.* **279**, 18392–18400 (2004).
117. Ioannou, M. S. et al. DENND2B activates Rab13 at the leading edge of migrating cells and promotes metastatic behavior. *J. Cell Biol.* **208**, 629–648 (2015).
118. Apolloni, A., Prior, I. A., Lindsay, M., Parton, R. G. & Hancock, J. F. H-ras but not K-ras traffics to the plasma membrane through the exocytic pathway. *Mol. Cell Biol.* **20**, 2475–2487 (2000).
119. Zawistowski, J., Sabouri-Ghomi, M., Danuser, G., Hahn, K. & Hodgson, L. A RhoC biosensor reveals differences in the activation kinetics of RhoA and RhoC in migrating cells. *Plos One* **8**, e79877 (2013).
120. Yang, S. S., Van Aelst, L. & Bar-Sagi, D. Differential interactions of human Sos1 and Sos2 with Grb2. *J. Biol. Chem.* **270**, 18212–18215 (1995).
121. Healy, K. D. et al. DLC-1 suppresses non-small cell lung cancer growth and invasion by RhoGAP-dependent and independent mechanisms. *Mol. Carcinog.* **47**, 326–337 (2008).
122. Wu, B. et al. Synonymous modification results in high-fidelity gene expression of repetitive protein and nucleotide sequences. *Genes Dev.* **29**, 876–886 (2015).
123. Nalbant, P., Hodgson, L., Kraynov, V., Toutchkine, A. & Hahn, K. M. Activation of endogenous Cdc42 visualized in living cells. *Science* **305**, 1615–1619 (2004).
124. Spiering, D. & Hodgson, L. Multiplex imaging of Rho family GTPase activities in living cells. *Methods Mol. Biol.* **827**, 215–234 (2012).
125. Spiering, D., Bravo-Cordero, J. J., Moshfegh, Y., Miskolci, V. & Hodgson, L. Quantitative Ratiometric Imaging of FRET-Biosensors in Living Cells. *Methods Cell Biol.* **114**, 593–609 (2013).
126. Dempsey, G. T., Vaughan, J. C., Chen, K. H., Bates, M. & Zhuang, X. Evaluation of fluorophores for optimal performance in localization-based super-resolution imaging. *Nat. Methods* **8**, 1027–1036 (2011).
127. Pertz, O. & Hahn, K. M. Designing biosensors for Rho family proteins—deciphering the dynamics of Rho family GTPase activation in living cells. *J. Cell Sci.* **117**, 1313–1318 (2004).
128. Efron, B. & Tibshirani, R. *An Introduction to the bootstrap*. Vol. xvi (Chapman & Hall, 1993).
129. Shannon, C. E. & Weaver, W. The mathematical theory of communication. (University of Illinois Press, 1949).
130. Zhou, Z. N. et al. Autocrine HBEGF expression promotes breast cancer intravasation, metastasis and macrophage-independent invasion in vivo. *Oncogene* **33**, 3784–3793 (2014).

Acknowledgements

This work was supported by an American Cancer Society Lee National Denim Day Postdoctoral Fellowship [PF-15-135-01-CSM (S.D.)]; NIH grants [CA100324 (J.E.S.), T32GM007288 (S.P.H.M.) and R35GM136226 (L.H.)]. STORM imaging was conducted in the Albert Einstein College of Medicine Analytical Imaging Facility, funded in part by the NCI Cancer Center grant P30CA013330. The Nikon Superresolution microscope (N-STORM imaging system) was purchased with the NIH grant SIG 1S10OD18218-1. Visitron Orbital-200 Ring-TIRF system was purchased with the NIH grant administrative supplement to R35GM136226. J.E.S. is the Betty and Sheldon Feinberg Senior Faculty Scholar in Cancer Research. L.H. is an Irma T. Hirschl Career Scientist. We thank members of the Condeelis, Segall, and Cox laboratories at Albert Einstein College of Medicine for their helpful discussions.

Author contributions

M.H., S.K.D. and L.H. conceived the project. M.H. and L.H. designed experiments. M.H., V.D.M., C.S., S.K.D. and L.H. performed the experiments. M.H. and L.H. analyzed the results. P.V.V. and L.H. designed the biosensors and characterized the biosensors. S.P.H.M., J.E.S. and L.H. performed the metastasis assays. L.H. directed the project. M.H. and L.H. wrote and revised the paper. All authors reviewed the paper and provided feedback.

Competing interests

The authors declare no competing interests.

Additional information

Supplementary information The online version contains supplementary material available at https://doi.org/10.1038/s42003-021-02583-3.

Correspondence and requests for materials should be addressed to Louis Hodgson.

Peer review information *Communications Biology* thanks Thomas Daubon, Bo Liu, and the other, anonymous, reviewers for their contribution to the peer review of this work. Primary Handling Editor: Christina Karlsson Rosenthal.

Reprints and permission information is available at http://www.nature.com/reprints

Publisher's note Springer Nature remains neutral with regard to jurisdictional claims in published maps and institutional affiliations.